Exploring short time-scales of a levitated nanosphere

Carlos Luis Alarcón Robledo

Master's thesis

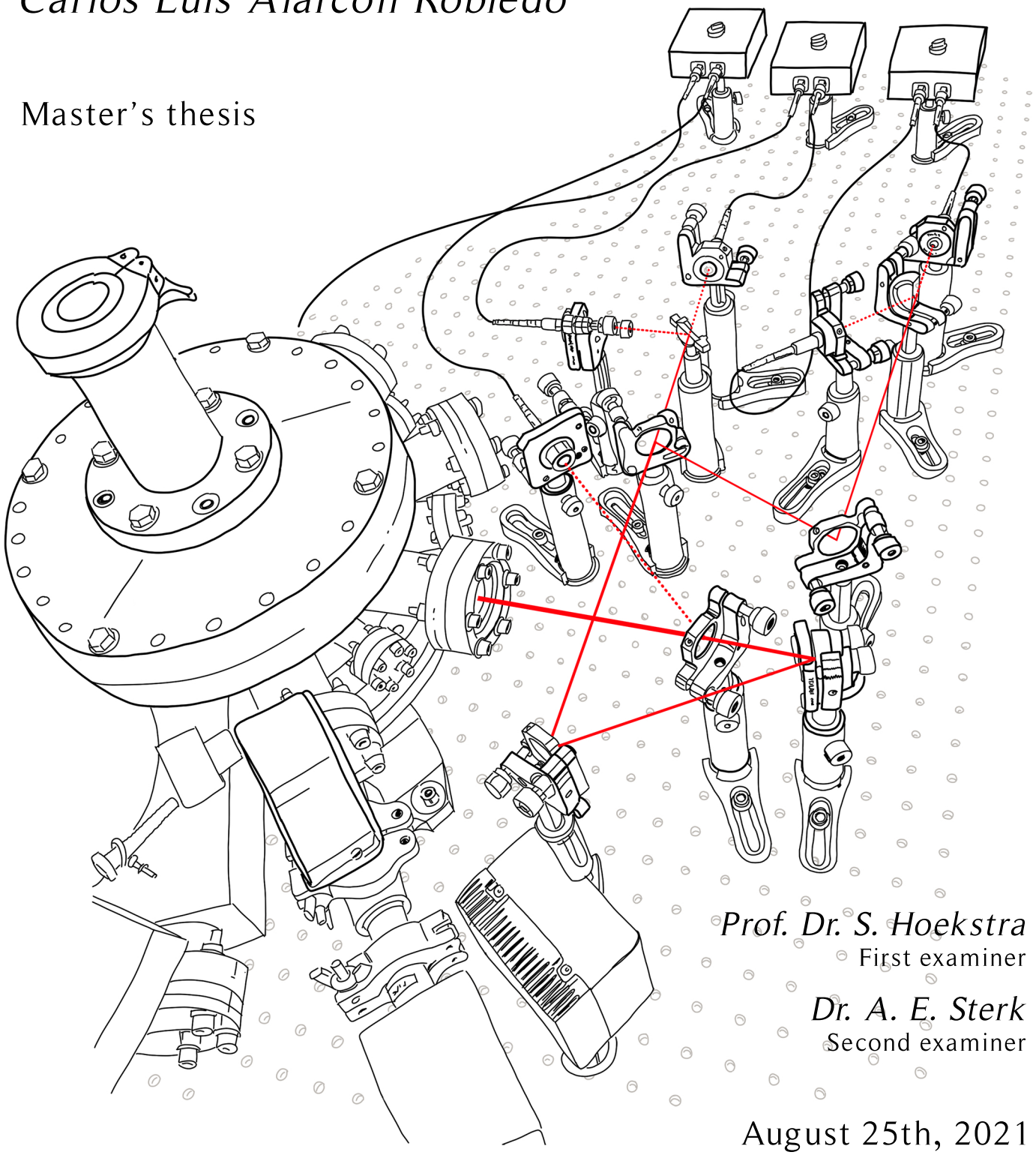

Prof. Dr. S. Hoekstra
First examiner

Dr. A. E. Sterk
Second examiner

August 25th, 2021

university of groningen / faculty of science and engineering / van swinderen institute for particle physics and gravity

Contents

Chapter 1

Introduction and motivation.

1.1 Levitated nanospheres, an introduction.

Experiments of levitated nanoparticles nowadays are possible thanks to a complex and a big configuration of scientific studies that include discoveries from the last years and make use of elemental principles postulated hundreds of years ago. They are feasible thanks to the advance in research of optomechanics, a discipline that explores the interactions of electromagnetic fields to control the motion of micro and nano-objects [1].

Tests of levitated particles are referred as a specific type of experimental configuration of Optical Tweezers (OTs) where a single laser beam traps nano/micro particles in gas, being usually air or high vacuum. Due to the low viscosity of the gas a strong optical force is needed to trap the objects inside the optical trap in order to counteract gravity. For that reason the single beam is strongly focused generating a gradient in the intensity of the laser that leads to gradient forces through the interaction of the laser electric field with the electric dipole of the particles. The size of the focused beam determines the size of the optical potential well while the particle charge polarizability and gradient of the laser intensity determine its depth.

During the next section we will go across a historical introduction to understand the relevance of OTs, its applications and the place that levitated particles take in this context. Next we will go deep into levitated particles experiments and specifically into two of their main applications related to the goals of our research group: First, their use as excellent mechanical resonators to measure weak forces and vibrations, and second their value as ideal sensors to study thermodynamics at the micro and nano-scale.

Among the different purposes, the main goal of this project is to illustrate the groundwork to pursue the first acceleration to date of the relaxation to equilibrium of a levitated nanoparticle from one stationary state to another. The end of the first chapter contains further information about the goals and the outlook of the thesis.

1.1.1 Towards levitated nanoparticles. Context:

A primary principle in levitation is the use of light momentum originating radiation-pressure forces. In the 17th century Kepler first postulated this concept while observing that the tails of comets point away from the sun. Maxwell predicted them for the first time and Lebedew, Nichols and Hull tested them in the 19th century. The statistics of the radiation-pressure force fluctuations were experimentally derived by Einstein in the 20th and Frisch and Beth demonstrated in the same century that linear and angular momentum transfer photons to atoms and macroscopic objects.

Most of the first key steps towards levitated particles experiments were developed by Arthur Ashkin in his work during the 1970s and 1980s with the invention of optical tweezers. His first work demonstrated that radiation-pressure forces from laser beams can be used to create stable traps and accelerate micro-sized particles [2]. In the later years he improved the stability of the system, implemented feedback [3] and discoverd the principle that we use to trap nanoparticles in our laboratory. He developed the first single-beam gradient force optical trap for dielectric particles [4] exploring also levitated particles in high vacuum. He furthermore trapped different kind of particles like atoms, liquid drops or neutral particles. These studies gave birth to several research fields that nowadays focus on the different applications that OTs can reach depending on the object that is trapped, the optics configuration and the regime that is explored. The broad impact of the invention of optical tweezers lead him to win the Nobel Prize in Physics in 2018.

The work of Ashkin has been refined during the last decades and its multiple applications have become apparent [5]. Within physics a large amount of studies have been devoted to the understanding of the different posibilites to induce distinct motions to the trapped object, such as the study of the inference of optical angular momentum. In this thesis we devote part of our work to this field applying external modulations on the intensity and the polarization observing the effects on the dynamics of our silica particle. See appendix C for experimental results and a theoretical discussion in 2.5 and 2.3.3.

In addition, OTs systems like levitated nanoparticles can be used as mechanical resonators thanks to their high quality factors being of great use in frequency and force sensing experiments. They are also the most promising systems to study thermodynamics at a micro- and nanos-cale which still lacks total understanding beside its great improvement in the last years. We leave the discussion of these applications for the next section where we discuss them in greater depth due to their relevance within the interest of our group.

It is of historical importance to mention the capability of OTs to measure the motion and dynamics of brownian particles. These motion was first described by Richard Brown in 1827 as the random movement of particles suspended in fluid when he studied with a microscope the dynamics of pollen particles on water. It was nevertheless Einstein after his PhD work in 1905 who first predicted brownian motion at

times longer than the momentum relaxation time of the particle. For these times he derived an expression of their mean square displacement. Furthermore he stated the equipartition theorem of statistical mechanics but wrongly concluded that due to the fast relaxation of the motion, the instantaneous velocity of a brownian particle would not be possible to measure in practice.

The pioneer study of Li [6, 7] refuted this statement measuring ballistic motion of micro-beads in air for the first time. This is the motion of a particle at times shorter than the momentum relaxation time of the system $\tau_p = m/\gamma = 2\pi/\Gamma$, where m is the mass of the particle, γ the Stokes friction coefitient and Γ the angular damping coefficient. The work showed for the first time the coupling of the trapped object to the thermal environment in a low-pressure underdamped regime. It was the first time that the motion coupled to the damping rate of the air molecules Γ_{air} was tested showing that the dynamics were driven by thermal noise.

The work inspired future research studies of levitated systems such as the first measurement of the coupling to photon recoil noise [8], where the damping rate is driven by the photon noise Γ_{photon} due to reaching a pressure of $10^{-8} mbar$ that makes the influence of Γ_{air} neglectable. It also inspired the first test of Kramers turnover [9] where the transition of the particle from one well to another is subject to the thermal noise of the air molecules Γ_{air}. Depending on the height of the barrier that separates the wells, only selective pressures can provide an appropriate damping rate to surpass the barrier.

More applications of OTs include the study of the complex dynamics of optically bounded trapped particles. Counter propagating beams can create optical wells of much larger size than the trapped particles capturing more than one particle at the same time. By trapping dielectric particles, light can generate forces between particles optically binding them. To end with physics applications we can also find studies of hydrodynamics and rheology with the use of OTs.

Furthermore OTs find their greatest applications within biology. It has been of use for the study of cells, DNA structures, DNA dynamics, molecular motors, motility and motion of swimming microorganisms and scanning probe microscopy.

1.1.2 Levitated nanoparticles in sensing experiments

Levitation experiments are distinguised from other OTs configurations by the fact that the laser is strongly focused and the object is suspended in air or high vacuum. This combination helps to avoid dissipation of the object with its environment allowing for a better isolation and a non-tethered oscillator to the environment [10]. Dissipation on the system can arrive from the surrounding gas and from the noise of the optical field. The isolation allows for high quality factors making them excellent candidates to measure forces and external vibrations as resonators.

A resonator is a system that exhibits resonance behaviour with an external signal. In other words, when an external signal is implemented at a frequency that matches a resonant mode of the frequency of the trapped oscillator or a small range close to its value, then it resonates with it making its amplitude oscillations greater.

Levitated nanoparticles can be used as mechanical resonators thanks to their high quality factors being of great use in frequency and force sensing experiments. The quality factor describes if an oscillator is underdamped or overdamped and by how much, and it depends on the damping term Γ_{CM} and the frequency of the trapped object Ω_{CM}. It is defined as $Q = \frac{E_{peak}(0\to T)}{E_{Lost}(0\to T)} = \frac{\Omega_{CM}}{\Gamma_{CM}}$ and also measures the ability of a system to store energy. Its value leads to completely different dynamical behaviors of the particle. For a driven damped harmonic oscillator, the dynamics are overdamped when $Q < 1/2$ while they are underdamped when $Q > 1/2$.

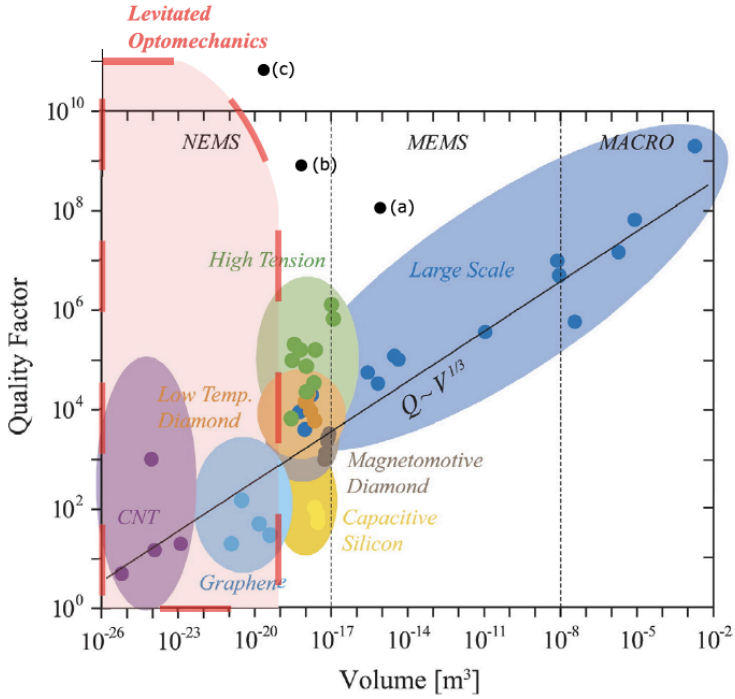

Figure 1.1: Dependence of quality factor on the volume of the oscillator. Levitated experiments operate in the red shaded area. Black points represent nowadays tethered optomechanics experiments. Picture obtained from reference [11]

An interesting comparison of the quality factors of different resonators was made by Millen [10], where he compared levitated optomechanical resonators with previously used resonators such as tethered optomechanical or tethered electromechanical resonators. See figure 1.1. While the quality factor of previously used resonators scales linearly with the cube root of the particle volume, this is not the case for levitated nanoparticles.

Because promising resonators require low masses and high quality factors, breaking

the mentioned trend makes levitated particles ideal for sensing experiments. As it is shown in figure 1.1 levitated particles can have at the same time both high quality factors and low volume, and mass is inevitably related to the volume through the density of the element. In short, levitated nanoparticles quality factors do not follow the general trend of scaling linearly with the cube root of the volume allowing them to be used as execelent resonators to sense forces. See section 2.6 for a further discussion on the minimum forces that any resonator and levitated particles can measure.

Since the quality factor of resonators is directly influenced by dissipation with the environment, extremely isolated systems such as levitated particles allow for high quality factors. Their very first limitation has to do with the coupling of the particle to the thermal environment where, at high pressures, the damping term is governed by the thermal noise Γ_{air}. Nevertheless, as lower pressures are reached the particle can be coupled to photon recoil noise, where the damping rate is driven by the photon noise Γ_{photon}. In a paper by Vijay Jain *et al*, [8] they coupled the particle to photon noise at a pressure of 10^{-8}mbar. Furthermore, external modulations can be used to change the damping rate of the center of the mass and also its effective temperature. This field is still under research and in this thesis we discuss some of the possibilities to modulate such dynamics with external modulations, see section 2.3.3 and 2.5.

Working in air and a vacuum is nevertheless more challenging since the damping term helps to stabilize the system and therefore while going to low pressures and reducing this term losses of the particle are very common.

1.1.3 Levitated nanoparticles on thermodynamics applications

The first work to investigate thermodynamic processes with OTs was the optical realization of a thermal ratchet where they modulated periodically in space the potential of a trapped brownian particle immersed in water [12]. Due to the necessity to test the later foundation of stochastic thermodynamics and fluctuation theorems [13] the research field grew in the last years.

Optically trapped micro/nano particles are ideal motion sensors of thermal fluctuations and therefore convenient for studying stochastic thermodynamics thanks to two characteristics.

The first is that the energy of the trapped object is comparable to the thermal fluctuations of the environment being of the order of k_BT. The second is the low amount of degrees of freedom necessary to describe their motion (usually only translational degrees of freedom of the center of mass) which through the central limit theorem allows for quantifying the energy fluctuations: For an extensive macroscopic quantity U (like heat, work or entropy production) with variance σ^2 and mean value $\langle U \rangle$, the cenral limit theorem allows that when a low amount of degrees of freedom

describes the system: $\rightarrow \langle U \rangle \sim \sigma^2$ [11].

These two properties make it possible to quantify their energy fluctuations and test macroscopic thermodynamical quantities. Most of the research done in the last years was done with colloidal particles trapped in liquid where the overdamped regime can be explored. But the underdamped regime lacks experimental results and is of fundamental interest as well.

Levitated nanoparticles are trapped in gas or a vacuum and by trapping them in a vacuum chamber, the coupling to the bath can be changed by changing the pressure of the surrounding gas. This allows for exploring different scales of the underdamped regime. Similarly to colloidal particles, levitated nanospheres can detect stochastic behaviour since the relative fluctuations of microscopic variables become comparable to their mean value. A recent literature review on the exploration of thermodynamics in the underdamped regime is given by J. Gieseler [14].

Examples of studies with levitated particles are the study of equilibration processes on experimentally accessible timescales verifying fluctuation equations [15,16]. Fluctuation theorems are exact relations that describe statistical properties of the fluctuations of macroscopic thermodynamic quantities (like heat, work and entropy production). In reference [15] with the help of feedback cooling, Gieseler *et al* prepare an initial steady state and investigate the fluctuations towards equilibrium during the transition to a new steady state where feedback cooling is switched off. They check a fluctuation theorem that quantifies the probability of observing second law violations while observing fluctuations of the energy on very short timescales before the fluctuations average out.

The possibility that OTs offer to alter the trapped optical potential allows additional scenarios with thermodynamical interests. Important studies involve the acceleration to equilibrium of a brownian particle from one state to another [17], the design of heat engines [18], or the creation of multiple-stability states like a double-well optical potential to test information thermodynamics [19], or kramers turnover [9]. In the next section we will specify within the applications of the first two since they are related to the direction of this project.

1.2 Motivation. Speeding-up relaxation and heat engines with levitated particles

The first of the previously mentioned possibilities lies within the main goal of this project, which is to create the groundwork to pursue the acceleration of the relaxation to equilibrium of a levitated particle through techniques reminiscent to short-cuts to adiabaticity (see section 2.7).

Relaxation processes toward equilibrium with levitated particles were already mea-

sured by Gieseler *et al* [15], nevertheless they have never been accelerated. Protocols to speed-up relaxation towards equilibrium that were tested by Ignacio A. Martinez [17] in the overdamped regime need to be tested in the underdamped regime [20]. In figure 1.2 we can observe the scheme of an acceleration technique towards equilibrium by Ignacio A. Martinez [17]. This experiment is of importance since it served as inspiration for our own project with levitated nanoparticles.

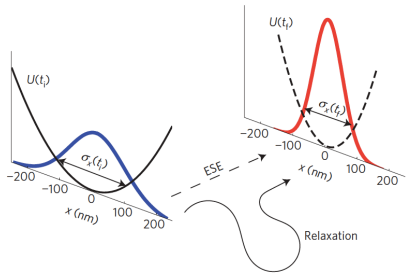

Figure 1.2: Sketch of a relaxation process where the stiffness of the optical potential is increased and the position distribution is studied. The particle is initially at equilibrium inside a potential well $U(t_i)$ (black line) with constant stiffness. The initial position distribution with variance $\sigma_x(t_i)^2$ is shown in blue. The stiffness is later increased and the particle therefore suffers a transitory process towards a new stationary state. The new stationary state differs from the first in a higher stiffness of the final optical potential $U(t_f)$ (represented with dashed lines). The position distribution with variance $\sigma_x(t_f)^2$ of the final state is shown in red. The process between the two stationary states is non-stationary and is the particle behaves stochastically with high fluctuations of its macroscopic variables. In this case a reminiscent technique to shortcuts to adiabaticity called Engineered Swift Equlibration (ESE) is used (see section 2.7). Figure obtained from reference [17].

By implementing such protocols we would be able to control the state of a levitated nanosphere on unprecedented timescales reaching equilibrium hundreds of times faster than the natural equilibrium rate. In addition, the realization of a shortcut has direct applications in sensing experiments causing transitory cancellation of resonance signals [18], in the driving of mesoscopic chemical or biological processes, and in the design of efficient nanothermal engines.

The realization of a shortcut can modify the signal to noise ratio (SNR) scheme helping to improve sensing tests of a certain frequency. When a shorcut process is implemented within a time shorter than a specific resonance, it leads to the transitory cancellation of the resonance signal [18]. It is a transitory process due to the equipartition theorem. The shortcut causes an energy transition from the selected resonance to the rest of the modes and degrees of freedom of the system. In our particular case currently we detect three degrees of freedom related to center of mass motion along the three directions in which the nanosphere can move. Therefore a short-cut would cause an energy transition from one selected degree of freedom to another. Nevertheless, additional degrees of freedom can be found in particles with anisotropic geometry, which polarizabilities (described by a tensor) change with the polarization vector of the light field. In the case of, for instance, a nanodumbell the

linear, circular or elliptical polarization, can inject rotation, torsion or a combination of both respectively on the trapped object [21, 22].

Heat engines have been developed in the overdamped regime with colloidal particles but not in the underdamped regime. It is of interest to do so since the dynamics of the trapped object are influenced by inertia effects that cannot be detected in the overdamped regime. Therefore the study of heat engines with levitated particles can help to discover sources of irreversibility in colloidal heat engines. Due to the stochastic behaviour of nano/micro particles trapped in optical wells, it is possible that heat nanomotors could run in reverse [14]. Identifying these sources would help in designing more efficient engines. While measurements of the momentum distribution is very challenging in the overdamped regime it is very accesible in high vacuum [6, 23].

A colloidal stochastic heat engine converts heat flow into mechanical work operating under a cyclic process. The cycle contains two isothermal processes where there is a variation of the potential to extract or implement work and two adiabatic processes with an instantaneous reduction/increase in temperature, see figure 1.3.

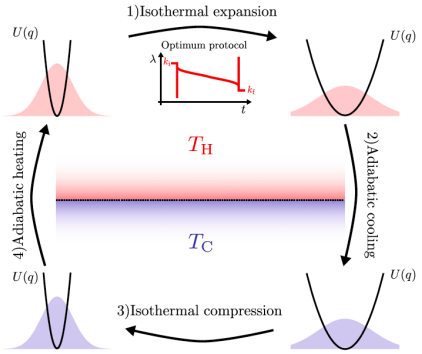

Figure 1.3: Stochastic heat engine cycle. A heat engine converts heat flow into mechanical work operating under a cyclic process. The cycle contains two isothermal processes where there is a variation of the potential to extract or implement work and two adiabatic processes with an instantaneous reduction/increase in temperature. Obtained from reference [11].

Compression and expansion is achieved by modifying the potential of the harmonic potential that traps the nanospheres by increasing or decreasing it respectively. Heating and cooling is done by changing the effective temperature of the center of motion particle.

There is a maximum efficiency that a heat engine in contact with two baths of temperatures T_C, T_H can reach determined by the second law of thermodynamics. It is the so-called Carnot efficiency $\eta_C = 1 - \frac{T_C}{T_H}$. This efficiency is believed to only be achievable when there is a zero power output without ejecting any work on its surroundings. Therefore for practical applications, experimentalists are interested in the efficiency at maximum output power.

The efficiency of a heat engine at maximum output power is limited by the Novikov-Curzon-Ahlborn efficiency [24, 25] $\eta = 1 - \sqrt{\frac{T_C}{T_H}}$, which is smaller than the Carnot efficiency setting a higher limit. Shortcuts to adiabaticity could be used in the adiabatic processes of a heat engine accelerating the usual slow driving. This raises the question among the scientific community on whether they could help to surpass the Novikov-Curzon-Ahlborn limit and for that reason a special attention has been devoted to the study of shorcuts in recent years.

Shorcut methods used with colloidal particles implement non-trivial functions to an input parameter (usually optical potential stiffness) of the equation of motion in order to optimize a process. These functions are usually found through the so-called *reversed philosophy* where instead of solving the equations of motion as usual (inputs i.e. stiffness give outputs i.e. position distributions), an imposed and desired solution of the equation gives back only certain possibilities of possible input parameters of the potential stiffness. In the case of speeding-up relaxation processes the non-trivial input function is implemented in the stiffness and is found such that the relaxation is shorcuted as much as possible [17]. Nevertheless, in the design of efficient heat engines the input function is found such that the adiabatic processes of a full cycle give maximum efficiency [26, 27], see sections 2.7 and 2.8 for a detailed explanation of the process.

In the overdamped regime a clear example is the work of Ignacio A. Martinez who, in addition to study the acceleration of relaxation processes, explored stochastic heat engines [28]. He developed together with J.M.R. Parrondo a Carnot engine [29] where the efficiency at maximum power matched the Novikov-Curzon-Ahlborn limit and where for certain conditions and short cycles they surpassed the Carnot bound.

While in the underdamped regime there have not been experimental attempts yet, there are theoretical proposals that are of interest with levitated nanospheres [26, 27]. It is wondered whether efficiency-power trades could surpass the Novikov-Curzon-Ahlborn bound. Levitated particles can check these trades in large regions and controlling the effective temperature much more precisely than colloidal particles. This is due to the possible combination of the control of gas pressure, feedback cooling and external driving that could allow for the creation of non-thermal baths to also surpass the Carnot efficiency [14].

Finally high vacuum avoids heating and decoherence from air molecules collisions allowing the study of quantum physics and producing quantum mechanical systems. Operating in the quantum regime can allow for the exploration of the possibility of attaining Carnot efficiencies in heat engines [30] or surpassing the Carnot limit [31].

1.3 Goals and Outlook of the project

The work hereby presented has the goal to set the foundations to pursue the first experimental implementation of a shortcut on the relaxation to equilibrium of a levitated particle. This requires two fundamental steps:

1. On the one hand precise knowledge of the relaxation time and the damping rate of the system. Therefore this is the first specific goal of our project: to obtain the relaxation time of the nanoparticle and verify it by measuring the position and velocity of a levitated nanoparticle at equilibrium within timescales shorter and longer than its relaxation time. This implies the detection of ballistic brownian motion [6, 7].

2. On the other hand a relaxation towards equilibrium requires to observe the transitional non-equilibrium dynamics between two distinct equilibrium states. For this reason the second goal of our project is to observe this relaxation by compression and decompression of the optical potential stiffness. The change on the stiffness is done with a step function between two constant values. In the future the change could be done with a polynomial function obtained by ESE techniques in order to accelerate the relaxation [17].

Furthermore an effort was dedicated in this work to look into the possibilities to implement modulations experimentally and how they result in the center of mass dynamics and temperature of the particle (see sections 2.5 and 2.3.3).

A good knowledge of the possibilities that external modulations offer to change the dynamics of levitated particles, will open the gate to new research questions as well as facilitate the pursuit of specific research goals. What does a levitated particle system have to offer? What characteristics of its dynamics can we change externally through modulations and forces? What research goals can we pursue through the control of their dynamics? What level of control can we achieve?

Being the initial goal of the group to pursue the use of levitated particles as mechanical resonators in order to measure weak forces and vibrations, I dedicated a part of my work to understand how external modulations could lead to force sensing schemes.

The combination of distinct modulations provide differential equations with non-trivial stability schemes that are of interest to study with methods related to the theory of dynamical systems and chaos. As an example, a combination of external modulations can create instability regions that lead to interesting sensing schemes of weak forces with levitated particles [32]. Also although a complex combination of modulations usually leads to non-solvable equations of motion, in occasions it is possible to obtain analitically the PSD of such equation through averaging methods [33]. Our group is under a collaborative effort with the Bernuilli Institute and

the group of Alef Sterk. The initiative aims to study the stability of the system of levitated particles under the framework of dynamical system and chaos. For mor detailed information on this aspect read section 2.5.3.

The goal of this project is the result of a literature research. It is a suitable question for our experiment that has not been pursued yet, see appendix A for the details. Protocols related to the theory of shortcuts to adiabaticity that were tested by Ignacio A. Martinez [17] in the overdamped regime need to be tested in the underdamped regime [20]. This regime can be explored by levitated nanospheres in high vacuum [15]. Through an inverse engineering the thermalization can be shortcutted in the compression or decompression of a harmonic oscillator from an angular frequency Ω_i to Ω_f, getting an exact scaling solution of the underdamped Fokker-Planck equation. See section 2.7 for more information.

By implementing such protocols we would be able to control the state of a levitated nanosphere on unprecedented timescales reaching equilibrium hundreds of times faster than the natural equilibrium rate. Furthermore the realization of a shortcut has direct applications in the design of efficient nanothermal engines, in the driving of mesoscopic chemical or biological processes and in sensing experiments.

1.3.1 Timetable and specific tasks

During the first months, September - December and January, I focused my efforts on familiarizing myself with the laboratory environment as well as, together with my PhD tutor, doing experiments at different pressures, polarizations and power in order to read out the dynamics of the particle (see appendix C). Nevertheless, the focus of my work during these months was devoted to reading the literature with the goal of finding a suitable research question to test experimentally with the current setup and the new implementation of an electric optical modulator (EOM) and a picoscope (see appendix A). During these months, I studied as well the result of external modulations in the differential equations that describe the dynamics of a levitated particle. (see sections 2.5 and 2.3.3).

From February on, I focused my effort on reading the relaxation behaviour of the levitated particle. I learnt from my PhD tutor how to perform experiments developing some of them on my own and reading the motion of the particle at a few $mbars$ with the use of a picoscope, a function generator and an electric optical modulator. I studied the principles and how to work with these three new devices and planned on my own the parameters to select in the picoscope and the functions to implement in the wave generator in order to develope experiments at low pressures. Additionally an incessantly alignment of the laser into the photodiodes was necessary.

Specific troubles that I treated on my own, apart from the literature study, are for instance coupling the laser beam to a maintaining polarizing fiber through the EOM in order to get a higher amount of power (see appendix B) or overcome to

problems of the chiller that cools the laser. Moreover I met a bachelor student weekly to provide advise in the development of simulations with the line of the project.

Chapter 2

Theory

In this section we will give first the general equation of motion of the center of mass of levitated nanoparticles influenced by both deterministic and stochastic forces. Next we will explain the optical deterministic forces that make them levitate as well as the stochastic forces that drive their motion inside the optical potential and are responsible for their damping term and its coupling to a thermal bath.

Once the basic framework is given, the dynamics will be described through their differential equation of motion which was derived by Langevin in the 20th century. We explain how experimental inputs result in new terms on the equation of motion that can help to control their motion: for instance modulated potentials, feedback cooling or parametric and direct driving. The broad amount of number of tools to modify their motion motivate studies of the stability of these complicated equations as well as pursue analytic and numerical solutions.

At the end of the section we give the general framework of shortcuts to adiabaticity in levitated particles and more specifically of the Engineered Swift Equilibration (ESE) method as well as the basic theory of heat engines for systems of levitated particles.

2.1 General formalism

A nanoparticle contains up to 10^{10} degrees of freedom. One can compare the size of its radius R with the radius of the atoms that it is made of R_0 in order to roughly compute $(R/R_o)^3 \approx 10^{10}$. Nevertheless, for practical reasons its behaviour is characterized by its internal temperature and the motion of the centre of mass. We relate the other degrees of freedom to this one to understand its behaviour. The equation of motion of the nanoparticle center of mass is:

$$\ddot{\mathbf{r}}(t) + \mathbf{\Gamma_{CM}}\dot{\mathbf{r}} = \frac{1}{m}\left[\mathcal{F}_{\text{fluct}}\,(t) + \mathbf{F}_{\text{det}}(\mathbf{r}, t)\right]. \tag{2.1}$$

Where m is the mass of the particle, $\mathcal{F}_{\text{fluct}}$ stochastic forces and $\mathbf{F}_{\text{det}}$ deterministic forces. In the following section we want to identify how these forces can be

implemented in the experiment in order to modify specific behaviours of the nanoparticle. Experimentally both the thermal bath and the optical potential depth can be altered.

2.2 Optical forces

We levitate Silica spheres of 156 nm diameter with a laser of a wavelength of 1056 nm, being under the condition of the diameter being much smaller than the wavelength. This is called the Rayleight regime and under these conditions the optical forces are well known and can be simply formulated since the radiation-pressure force can be neglected. The origin of the force that traps the levitated particle counteracting gravity is electro-magnetical. The electric fields of the laser interact with the dipole of the particle generating a force governed by the gradient of the intensity of the laser and the complex polarizability:

$$\alpha\left(\lambda\right) = 4\pi\epsilon_0 R^3 \frac{\epsilon_{\mathrm{r}}\left(\lambda\right) - 1}{\epsilon_{\mathrm{r}}\left(\lambda\right) + 2}. \tag{2.2}$$

where ϵ_{r} is the permittivity related to the complex refractive index through $\epsilon_{\mathrm{r}}\left(\lambda\right) = n\left(2\pi c/\lambda\right)^2$. The polarizability can be divided in its real and complex parts $\alpha = \alpha^{'} + i\alpha^{''}$. While the real part determines the optical potential depth, the complex part is related to the absorption of photons.

The optical force that counteracts gravity can be expressed in the following formula where $\mathbf{E}$ is the electric field of the light:

$$\left\langle \mathbf{F}_{\mathrm{grad}} \right\rangle = \frac{\alpha'}{2} \left\langle \nabla \mathbf{E}^2 \right\rangle. \tag{2.3}$$

The system can be modelled as a harmonic oscillator and under the assumptions that the laser beam is Gaussian and that the Rayleight regime applies, the gradient force can be approximated as a linear resoring force:

$$\left\langle \mathrm{F}_{\mathrm{grad},q} \right\rangle = -\mathrm{k}_q q, \quad q \in \{x, y, z\}. \tag{2.4}$$

Where x, y are the spatial coordinates transverse to de direction of propagation of the laser beam and z the longitudinal direction. The spring constants k_q differ from each degree of freedom of the center of mass of the nanoparticle and for a linearly polarized Gaussian beam reads as:

$$\mathrm{k}_q = \frac{4\alpha' P_{\mathrm{opt}}(t, q, \dot{q})}{\pi c \epsilon_0 \mathrm{w}_x \mathrm{w}_y \mathrm{w}_q^2}. \tag{2.5}$$

Where w_q stands for the waist of the beam in the q direction. The waist along the longitudinal direction w_z is given by the so-called Rayleight range z_0 through $\mathrm{w}_z = \sqrt{2 z_0}$. Since the dynamics of the particle can be modified in terms of time and with the help of feedback also in terms of the position or the velocity of the

particle, the power within the optical field $P_{\rm opt}(t, q, \dot{q})$ has been included as a function of these variables. Due to the experimental possibilities it is usually varied around its mean value and in the literature its modulations are expressed as $P_{\rm opt}(t, q, \dot{q}) = P_0 + \delta P(t, q, \dot{q})$.

Thus as an example and an easy exercise we could perform an experiment to quantify the changes of the stiffness in terms of power. We could vary the power of the applied laser while we measure the changes in the frequency of the Fourier Transformed signal. Since the frequency of a harmonic oscillator depends on the stiffness of its potential as: $f_q = \frac{\sqrt{k_q/m}}{2\pi}$ the observed changes on the squared frequency at the noted values of applied power would give us the linear dependence between both quantities. Nevertheless, this method assumes that the dynamics of the particle are harmonic which is not always true, and the frequency of the particle can be measured only with certain uncertainty that depends on the pressure and the calibration method to obtain the results.

2.3 Stochastic forces

The optically trapped nanoparticle at high pressures is driven by thermal stochastic forces $\mathcal{F}_{\rm gas}(t)$ from the mechanical collisions of the air molecules that couple the particle to the air thermal bath. This is the main contribution of dissipation that defines the damping of the center of mass Γ_{CM} at pressures higher than 10^{-6} mbar. Nevertheless below that pressure we can find contributions to the damping of the center of mass motion from the light radiation and, in the quantum regime, noise driving wavefunction collapse. Furthermore it is possible to apply external modulations to influence Γ_{CM} through a feedback mechanism or stochastic driving.

Stochastic forces are characterized by their power spectral density (PSD) $S_{\rm ff}^{\rm n}$ where the index n is included to indicate any stochastic contribution. In most of the cases they are frequency independent (and therefore called as *white noise*) having autocorrelation functions $\langle \mathcal{F}_n(t)\mathcal{F}_n(t')\rangle = 2\pi S_{\rm ff}^{\rm n}\delta(t-t')$

After the so-called relaxation time $\tau = 2\pi/\Gamma_{CM}$ the particle reaches thermodynamical equilibrium at the effective temperature:

$$T_{\rm CM} = \frac{\pi S_{\rm ff}}{{\rm k_B} m \Gamma_{\rm CM}}. \tag{2.6}$$

Where the PSD and the damping term can include the contribution of the distinct stochastic forces that influence the particle $S_{\rm ff} = \sum_n S_{\rm ff}^{\rm n}$; $\Gamma_{\rm CM} = \sum_n \Gamma_{\rm n}$.

2.3.1 Gas damping

At pressures higher than 10^{-6} mbar the damping term related to the gas thermal bath where a spherical particle with radius R is immersed is:

$$\Gamma_{\text{gas}} = \frac{6\pi\mu_{\text{gas}}R}{m}\frac{0.619}{0.619+\text{Kn}}\left(1+c_{\text{K}}\right), \quad S_{\text{ff}}^{\text{gas}} = \frac{m\text{k}_{\text{B}}T_{\text{gas}}}{\pi}\Gamma_{\text{gas}}. \tag{2.7}$$

Where μ_{gas} is the viscosity coefficient $\mu_{gas} = 2\sqrt{m_{\text{gas}}\text{k}_{\text{B}}T_{\text{gas}}}/3\sqrt{\pi}\sigma_{\text{gas}}$. With value for air: $\mu_{gas} = 18.27\times10^{-6}$ kg(ms)$^{-1}$. The Knudsen number given by $\text{Kn} = \bar{l}/a$ where the mean free path is $\bar{l} = \text{k}_{\text{B}}T_{\text{gas}}/\left(\sqrt{2}\sigma_{\text{gas}}P_{\text{gas}}\right)$ and $\sigma_{\text{gas}} = \pi\text{d}_{\text{m}}^2$. The radius of air molecules is $\text{d}_{\text{m}} = 0.372nm$. Finally $c_K = 0.31\text{Kn}/\left(0.785+1.152\text{Kn}+\text{Kn}^2\right)$.

This expression is simplified under the Knudsen regime at pressures lower than: $P_{\text{gas}} \approx 54.4\text{mbar}/R(\mu\text{m})$. This this the case, since for a particle of radius $R(\mu\text{m}) \approx 0.1$ μm we are easily below pressures of $P_{\text{gas}} \approx 544$ mbar:

$$\frac{\Gamma_{\text{gas}}}{2\pi} = \frac{3}{\pi\sqrt{2}}\frac{\mu_v\sigma_{\text{gas}}}{\text{k}_{\text{B}}T_{\text{gas}}\,\rho}\frac{P_{\text{gas}}}{R}. \tag{2.8}$$

2.3.2 Photon shot noise damping

Below a pressure of 10^{-6} mbar an optically trapped particle experiences a stochastic force due to the noise of the discrete photons. It has been recently measured in reference [8] and the effective temperature of this bath can be calculated with eq (2.6). Its contribution to the damping term and the PSD of the particle are defined as:

$$\frac{\Gamma_{\text{rad}}}{2\pi} = c_{\text{dp}}\frac{P_{\text{scat}}}{2\pi mc^2} \text{ and } S_{\text{ff}}^{\text{rad}} = c_{\text{dp}}\frac{\hbar\omega P_{\text{scat}}}{2\pi c^2}. \tag{2.9}$$

With scattered power $P_{\text{scat}} = \sigma_{\text{scat}}\, I_{\text{opt}}$ and $\sigma_{\text{scat}} = |\alpha|^2k_{\text{L}}^4/6\pi\epsilon_0^2$. The factor c_{dp} takes its value depending on what is the direction of motion of the particle compared to the polarization of the laser. It is $c_{\text{dp}} = 2/5$ for motion along the direction of polarization and $c_{\text{dp}} = 4/5$ for perpendicular.

2.3.3 External modulated damping

The eq (2.6) represents an equilibrium state. When external modulations are applied injecting or extracting energy, the particle enters a non-equilibrium state and the relation does not hold anymore. Nevertheless, once the external modulation does not vary with time anymore, a new equilibrium must be reached within the relaxation time $\tau = 2\pi/\Gamma_{CM}$.

On the contrary if the external modulation is constantly applied in terms of time, the damping rate and the effective temperature can be modified independently. Due to the time-dependence of the external forces non-equilibrium stationary states can be reached. Such is the case of for instance the prepared state that Gieseler *et al*

prepared with parametric feedback cooling [15]. Here they manage as well to define an effective temperature of the "feedback bath" through the calculation of the average energy of the system.

There are many ways to implement feedback cooling, (see section 2.5.2) but ideally it damps the particle motion at a rate Γ_{fb} without adding fluctuating forces such that S_{ff}^{fb}=0. In that case it is called cold damping. Nevertheless, a real signal with feedback mechanism contains noise heating the particle.

A feedback cooling process changes both the effective temperature and damping rate of equation (2.13) a quantity $\delta\Gamma$ such that $\Gamma_{\mathrm{CM}} \rightarrow \Gamma_{\mathrm{eff}} = \Gamma_{\mathrm{CM}} + \delta\Gamma$. The effective temperature under the process is modified to:

$$T_{\mathrm{eff}} = T_{CM}\frac{\Gamma_{\mathrm{CM}}}{\Gamma_{\mathrm{CM}} + \delta\Gamma}. \tag{2.10}$$

Notice that the change of the damping term $\delta\Gamma$ determines how much the temperature changes and its sign if it increases or decreases.

As an opposite example, external stochastic forces would add fluctuating forces without providing any damping. In this case $\Gamma_{\mathrm{drive}} = 0$ and $S_{\mathrm{ff}}^{\mathrm{drive}} = q^2 S_{qq}$ where b is the coupling parameter to the control field and S_{qq} its spectral density. This can be realized for example with fluctuating electric fields, where q corresponds to the charge on the particle.

2.4 Equations of motion and dynamics.

In this section we will start our discussion centered on the later analysis of the control of the dynamics of a levitated particle. We will discuss free brownian motion and harmonic brownian motion and give the results of variance and PSDs that come out of the differential equations

2.4.1 Free brownian motion

The equation of motion of the dynamics of a free particle coupled to a thermal bath at temperature T_{CM} with rate Γ_{CM} was derived by Langevin in 1908 from Newtons second's law:

$$\ddot{q} + \Gamma_{\mathrm{CM}}\dot{q} = \mathcal{F}_q(t)/m. \tag{2.11}$$

Being $\mathcal{F}_q(t)/m = \sqrt{2\mathrm{k_B}T_{\mathrm{CM}}\Gamma_{\mathrm{CM}}/m}\Xi(t)$ and $\Xi(t)$ a normalised white noise process with $\langle\Xi(t)\rangle = 0, \langle\Xi(t)\Xi'(t)\rangle = \delta\,(t - t')$.

The equation of motion is driven by a stochastic force and therefore the motion of the particle is randomized. Nevertheless, one can define quantities as the mean square displacement given by [7]:

$$\sigma_q^2(t) = \left\langle [q(t) - q(0)]^2 \right\rangle = \frac{2\mathrm{k_B}T_{\mathrm{CM}}}{m\Gamma_{\mathrm{CM}}^2} \left[\Gamma_{\mathrm{CM}} t - 1 + e^{-\Gamma_{\mathrm{CM}} t}\right]. \tag{2.12}$$

At times longer than the relaxation time $t \gg 2\pi/\Gamma_{\mathrm{CM}}$ we obtain the result that Einstein obtained in his PhD work $\sigma_q^2(t) = 2Dt$ with diffusion coefficient $D = \mathrm{k_B}T_{\mathrm{CM}}/m\Gamma_{\mathrm{CM}}$. Nevertheless, at times shorter than the relaxation time inertia effects are observed obtaining ballistic motion $\sigma_q^2(t) = (\mathrm{k_B}T_{\mathrm{CM}}/m)\, t^2$. Notice that in the overdamped regime these effects are hardly observable since the relaxation time is given by $\tau = 1/\Gamma_{\mathrm{CM}}$

2.4.2 Harmonic brownian motion

Under the influence of an optical trap, the motion of the particle can be considered harmonic close to the center of the well i.e. the equilibrium position. From equation (2.3) one can use Newton's 2nd law to obtain that the center of mass of the particle follows brownian motion under the following differential equation:

$$\ddot{q} + \Gamma_{\mathrm{CM}}\dot{q} + \Omega_{0_q}^2 q = \sqrt{2\mathrm{k_B}T_{\mathrm{CM}}\Gamma_{\mathrm{CM}}/m}\,\Xi(t). \tag{2.13}$$

In this case, due to the confinement of the optical trap, the particle oscillates inside with frequency $\tilde{\Omega} = \sqrt{\Omega_0^2 - \Gamma_{\mathrm{CM}}^2/4}$. The frequency is different for each degree of freedom depending on the shape of the potential since the trap frequency is $\Omega_{0\mathrm{q}} = \sqrt{\mathrm{k}_q/m}$ and k_q given in eq (2.5).

As discussed in chapter 1, depending on the relation between the damping rate and the frequency of the particle, we can have overdamped, underdamped and critically damped case. For the underdamped motion of levitated particles, the mean square displacement of the position is given by:

$$\sigma_q^2(t) = \frac{2\mathrm{k_B}T_{\mathrm{CM}}}{m\Omega_0^2}\left[1 - e^{-\frac{\pi t}{\tau_p}}\left(\cos(\tilde{\Omega}t) + \frac{\pi\sin(\tilde{\Omega}t)}{\tau_p\tilde{\Omega}}\right)\right]. \tag{2.14}$$

Where $\tau_p = 2\pi/\Gamma_{CM}$ is the momentum relaxation time of the system. The autocorrelation function of the position is given as:

$$\langle q(t)q(0)\rangle = \frac{\mathrm{k_B}T_{\mathrm{CM}}}{m\Omega_0^2} - \frac{1}{2}\sigma_q^2(t). \tag{2.15}$$

And the autocorrelation function of the velocity as:

$$\langle v(t)v(0)\rangle = \frac{\mathrm{k_B}T_{\mathrm{CM}}}{m}e^{-\frac{1}{2}\Gamma_{\mathrm{CM}}t}\left(\cos(\tilde{\Omega}t) - \frac{\Gamma_{\mathrm{CM}}}{2\tilde{\Omega}}\sin(\tilde{\Omega}t)\right). \tag{2.16}$$

The power spectral density (PSD) is defined as the Fourier transform of the position autocorrelation function $S_{qq}(\Omega) = \int_{-\infty}^{\infty}\langle q(t)q(0)\rangle e^{i\Omega t}\,\mathrm{d}t$:

$$S_{qq}(\Omega) = |\chi(\Omega)|^2 S_{\mathrm{ff}}(\Omega) = \frac{\Gamma_{\mathrm{CM}}\mathrm{k_B}T_{\mathrm{CM}}/\pi m}{\left(\Omega^2 - \Omega_0^2\right)^2 + \Gamma_{\mathrm{CM}}^2\Omega^2}. \tag{2.17}$$

Where $\chi(\Omega) = m^{-1}\left[\Omega^2 - \Omega_0^2 + i\Gamma_{\mathrm{CM}}\Omega\right]^{-1}$ is the harmonic oscillator response function.

The PSD provides the Temperature T_{CM} and the damping rate Γ_{CM}, and the frequency spectrum of the autocorrelation function gives the trap frequency in its main peak.

The harmonicity of the motion is valid under the condition:

$$\frac{3k_{\mathrm{B}}T_{\mathrm{CM}}}{\mathrm{w}_q^2\Gamma_{\mathrm{CM}}\Omega_{0\mathrm{q}}M} \ll 1. \tag{2.18}$$

If this condition is not met, non-linearities of the potential must be taken into consideration linking the different motional degrees-of-freedom and making them not independent anymore.

2.5 Modulations and control of the dynamics.

Eq (2.13) assumed brownian harmonic motion of an optically trapped particle. In this section we will consider different scenarios that would add new terms to eq (2.13). We will discuss the possibilities that levitated experiments offer to alter its dynamics and effective temperature.

The combination of an electric optical modulator, a polarizer and a function generator offer infinite possibilities (see chapter 3) of functions in terms of time $f(t)$ that can vary the power of the laser and therefore the trap stiffness and the frequency of the trap. Notice that eq (2.5) suggests that the stiffness of the harmonic potential could be modulated through the laser power. This results in a time dependent trap stiffness and therefore trap frequency in eq (2.13) $\Omega_{0_q}^2 \to \Omega_{0_q}^2 f(t)$.

Furthermore the use of a feedback mechanism that reads the particle motion allow for implementing position or velocity dependent functions to the laser power. The feedback offer therefore, the implementation of position/velocity dependent functions $f(t, q, \dot{q})$. If the function is implemented to the laser power, then in eq (2.13) $\Omega_{0_q}^2 \to \Omega_{0_q}^2 f(t, q, \dot{q})$. Getting:

$$\ddot{q} + \Gamma_{\mathrm{CM}}\dot{q} + \Omega_{0_q}^2 f(t, q, \dot{q})q = \sqrt{2\mathrm{k_B}T_{\mathrm{CM}}\Gamma_{\mathrm{CM}}/m}\Xi(t). \tag{2.19}$$

Where the implementention of velocity dependent functions can lead to a change in the damping rate such that the new effective damping term would substitute Γ_{CM} in eq (2.13): $\Gamma_{\mathrm{CM}} \to \Gamma_{\mathrm{eff}} = \Gamma_{\mathrm{CM}} + \delta\Gamma$. Where $\delta\Gamma$ is the new contribution.

Additionally one could implement external electric or magnetic forces that interact with the particle independently of the optical trap. It is usual to test the force sensitivity of the oscillator through the implementation of these forces. Moreover it is possible to implement them with the use of feedback making them position/velocity dependent. For instance, applying an electrical feedback signal to electrodes placed

close the levitated charged particle [34, 35]. In these cases an external force is implemented:

$$\ddot{q} + \Gamma_{\mathrm{CM}}\dot{q} + \Omega_{0_q}^2 q = \sqrt{2\mathrm{k_B}T_{\mathrm{CM}}\Gamma_{\mathrm{CM}}/m}\Xi(t) + f_{\mathrm{ext}}(t, q, \dot{q}). \tag{2.20}$$

2.5.1 Power modulation

Experimentally an EOM can vary the power around a mean value P_0. We express it then as $P_{\mathrm{opt}}(t) = P_0 + \delta P(t)$. Where $\delta P(t)$ is the variation of the power through the EOM. This results in a time dependent trap frequency in eq (2.13) $\Omega_{0_q}^2 \to \Omega_{0_q}^2 + \delta k_q(t)/m$. Where $\delta k_q(t)$ stands for the variation on the stiffness through the laser power variation $\delta P(t)$ related through eq(2.5).

Furthermore the use of a feedback mechanism that reads the particle motion allow to implement position or velocity dependent functions to the laser power. The feedback offer therefore, the implementation of position/velocity dependent functions to the laser power $\delta P(t, q, \dot{q})$. In this case in eq (2.13) $\Omega_{0_q}^2 \to \Omega_{0_q}^2 + \delta k_q(t, q, \dot{q})/m$.

Then the general equation of motion of a particle in a thermal bath and confined in a modulated optical potential would read as:

$$\ddot{q} + \Gamma_{\mathrm{CM}}\dot{q} + (\Omega_{0_q}^2 + \delta k_q(t, q, \dot{q})/m)q = \sqrt{2\mathrm{k_B}T_{\mathrm{CM}}\Gamma_{\mathrm{CM}}/m}\Xi(t). \tag{2.21}$$

Such modulations implemented through the gradient force (see eq (2.3)) are generally called in the literature as "parametric", examples of it are parametric driving [36] or parametric feedback cooling [23].

In the case of parametric feedback cooling, Gieseler implemented a modulation dependent on position and velocity such that $f(t, q, \dot{q}) = 1 + \eta q\dot{q}/\Omega_0$ or following the new formalism: $\delta k_q(t, q, \dot{q})/m = \Omega_0^2 \eta q\dot{q}$, where η represents the feedback strength. This implemented fucntion is linearly velocity and position dependent but results in a non-linear modulation in the eq (2.21). The velocity dependence leads to not only the modification of the trap frequency but also to the change of the particle damping rate Γ_{CM}.

In the case of parametric driving, Gieseler implemented a time-dependent function in order to excite the particle injecting energy and allowing for large amplitude oscillations that could explore non-linearities of the optical potential. The implemented function was $f(t) = 1 + \epsilon\cos(\Omega_{\mathrm{m}}t)$ or in the new formalism $\delta k_q(t, q, \dot{q})/m = \Omega_0^2\epsilon\cos(\Omega_{\mathrm{m}}t)$ where the parameters, strength ϵ and frequency Ω_{m} of the modulation were controlled externally.

2.5.2 Feedback cooling

For the sake of generality since the center of mass motion of the particle could be modulated not only through the power of the laser but also through external forces

the feedback cooling $f_{\mathrm{fb}}(t)$ usually reads as an independent term in the equation of motion:

$$\ddot{q} + \Gamma_{\mathrm{CM}}\dot{q} + \Omega_0^2 q = \sqrt{2\mathrm{k_B}T_{\mathrm{CM}}\Gamma_{\mathrm{CM}}/m}\Xi(t) + f_{\mathrm{fb}}(t, q, \dot{q}). \tag{2.22}$$

In order to extract energy from the particle, the feedback term could be implemented linear to the velocity $f_{\mathrm{fb}}(t, q, \dot{q}) = A\dot{q}$ with optimized gain A. This is called cold damping since the motion is damped without any additional heating. Another option would be to add a term dependent on the position: $f_{\mathrm{fb}}(t, q, \dot{q}) = A_1\dot{q} + A_2 q$. such configuration was made by Ashkin [3] to improve the stability of the levitated particles.

As mentioned before, Gieseler implemented the so-called parametric feedback cooling [23] which differs from the previous cases in its nonlinearities. It was implemented through the gradient force (see eq (2.3)) with a modulation of the trapping potential. While in the previously discussed schemes the damping rate is independent of the oscillator energy, in this case the power is a function of the oscillator amplitude. Solutions of the variance and the PSD at steady states while applying this method can be found in his PhD thesis.

A feedback cooling process changes both the effective temperature and damping rate of equation (2.13) a quantity $\delta\Gamma$ such that $\Gamma_{\mathrm{CM}} \rightarrow \Gamma_{\mathrm{eff}} = \Gamma_{\mathrm{CM}} + \delta\Gamma$. The effective temperature under the process is modified to:

$$T_{\mathrm{eff}} = T_{CM}\frac{\Gamma_{\mathrm{CM}}}{\Gamma_{\mathrm{CM}} + \delta\Gamma}. \tag{2.23}$$

Notice that the change of the damping term $\delta\Gamma$ determines how much the temperature changes and its sign if it increases or decreases.

2.5.3 Non-linearities, direct and parametric driving

Until now, we have given the general formalism of how the implementation of external modulations results in the equation of motion. We have also discussed some of the most interesting applications when adding a velocity dependent term to implement feedback cooling to the motion of the particle. Here we will discuss further examples of functions in terms of time that have been used in recent studies. Their implementation can vary the motion of the particle in distinct manners and serve different purposes such as exploring non-linearities of the optical potential well, seeking sensitive force sensing schemes, designing bistability amplitude regions or studying the phenomena of stochastic resonance.

Parametric driving

As the adjective *parametric* indicates, parametric driving is a modulation in the optical potential in terms of time that drives the motion of the particle. A specific scheme was introduced by Gieseler where he used this term to drive the motion of the nanoparticle into non-linear regions of the optical potential well. In order to

study non-linearities, the particle must be driven to higher amplitudes. Jan Gieseler *et al* implemented a function in eq (2.19) such that $f(t) = 1 + \epsilon \cos(\Omega_m t)$, or in the previous formalism $\delta k_q(t, q, \dot{q})/m = \Omega_0^2 \epsilon \cos(\Omega_m t)$. The external parameters, strength ϵ and frequency Ω_m of the modulation were controlled externally. Such a modulation, can interact with the particle, altering its motion when selecting resonant frequencies with the center of mass trap frequencies $\Omega_m = n\Omega_0$. The highest resonance is at $n = 2$.

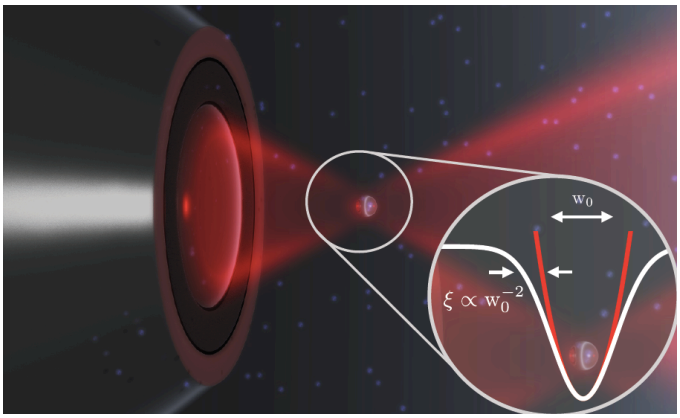

Figure 2.1: A strongly focused beam creates an optical potential with nonliniearities. The first order nonlinear term is well known as the duffing factor ξ and was measured by Gieseler with the help of a parametric driving that drove the particle with higher amplitudes to the non-linear parts of the potential.

In their study they excited the particle amplifying its amplitudes thanks to the modulation. This allowed them to reach the non-linearities of the optical potential and compute its duffing factor ξ. Introducing non-linearities into eq (2.13) as well as the parametric external modulation we get:

$$\ddot{q} + \Gamma_{CM}\dot{q} + \Omega_0^2 \left[1 + \epsilon \cos(\Omega_m t) + \xi q^2\right] q = \sqrt{2k_B T_{CM} \Gamma_{CM}/m}\,\Xi(t). \tag{2.24}$$

Studies similar to these can be carried out in the Stark decelerator of our laboratory where a modulation of the voltage implemented on the electrodes create anharmonic wells that trap samples of particles. Similarly to the study of Gieseler we could measure the non-linear terms of the Stark potential while applying parametric driving. Gieseler computed through secular perturbation theory the anharmonicities effects on the harmonic trap $\Omega_{\text{eff.}} = \Omega_0 \left(1 + \frac{3}{8}\xi q^2\right)$. In my bachelor thesis I computed through perturbation theory the non-linear terms of a general quartic potentil obtaining the same equation. Although an experimental effort was made to find the resonance of SrF with parametric driving, future steps could be implemented in order to compute the non-linearities of the Stark potential.

Direct driving.

Another example is the implementation of direct driving. In this case the modulation comes from an external force instead of from a modulation of the potential. The difference from the previous case is that the term in the equation of motion does not have to be necessary multiplied by the position term. An example of this modulation was done by Ricci implementing direct driving through external electric fields [37] in order to simulate an external force and study the sensing possibilities of the resonator for instance to measure mass. He used as well a sinusoidal function such that in eq (2.20) $f_{ext}(t) = \frac{F_0}{m} cos(\omega_{dr})$ where the controlled external parameters were the electric strength of the modulation F_0 and the frequency ω_{dr}. In this case the major influence is injected in the trapped particle when ω_{dr} is in resonance with the frequency of the trapped particle $\Omega_{\mathrm{m}} = n\Omega_0$ where the highest resonance is again $n = 2$.

Combination of modulations.

Finally it is also interesting to apply combined modulations. Ricci created an amplitude bistability region with the use of feedback cooling, direct driving and external noise [38]. Bistability regions have also been of application in order to compare the classical system to a quantum mechanical one [39], and have been explored not only with feedback cooling but also with cavity schemes [40].

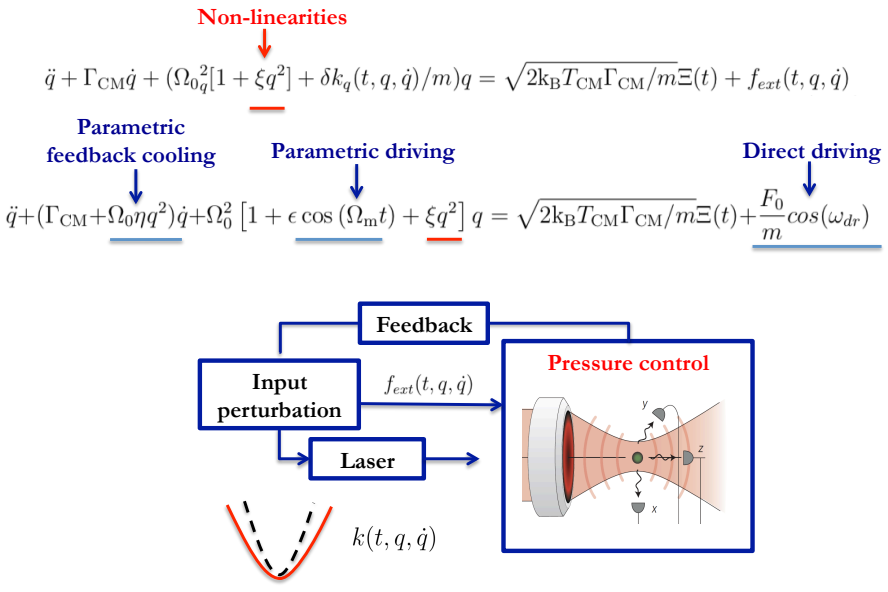

Figure 2.2: Scheme of the setup for combined modulations and the result in the equation of motion. While the first equation gives the general equation of motion the second gives specific examples of modulations discussed in the text.

Some theoretical efforts studied the stability of similar dynamical schemes to seek for the detection of weak forces with the use of resonators. Ricci implemented a direct driving scheme such that in eq (2.20) $f_{ext}(t) = \frac{F_0}{m} cos(\omega_{dr})$.The induced external force served to simulate a detectable force by the resonator and under these

conditions he obtained the minimum detectable force if a nano-oscillator in eq (2.28).

Similar studies can be a beautiful match between the interests of our group and the studies that the Bernuilli Institute and the group of Alef Sterk. A combination of external modulations can create instability regions that lead to interesting sensing schemes of weak forces with levitated particles [32]. In occasions it is possible to obtain analitically the PSD of such equation through averaging methods [33].
Ricci discussed in his PhD thesis the implementation of different modulations to infer bistability dynamics and explore what possibilities this would bring to improve force sensing with levitated particles, see fig 2.2.

The general equation including non-linearities read as:

$$\ddot{q} + \Gamma_{\mathrm{CM}}\dot{q} + (\Omega_{0_q}^2[1 + \xi q^2] + \delta k_q(t, q, \dot{q})/m)q = \sqrt{2\mathrm{k_B}T_{\mathrm{CM}}\Gamma_{\mathrm{CM}}/m}\Xi(t) + f_{ext}(t, q, \dot{q}). \tag{2.25}$$

And using parametric feedback cooling, direct driving as well as parametric driving we get:

$$\ddot{q}+(\Gamma_{\mathrm{CM}}+\Omega_0\eta q^2)\dot{q}+\Omega_0^2\left[1 + \epsilon\cos\left(\Omega_{\mathrm{m}}t\right) + \xi q^2\right] q = \sqrt{2\mathrm{k_B}T_{\mathrm{CM}}\Gamma_{\mathrm{CM}}/m}\Xi(t)+\frac{F_0}{m}cos(\omega_{dr}). \tag{2.26}$$

See figure 2.2 for clarity.

2.6 Force sensing

The minimum detectable force of a nano-oscillator is limited by the thermal energy of its center of mass as well as its mechanical quality factor:

$$F_{\mathrm{min}} = \sqrt{\frac{4\mathrm{k}_q k_{\mathrm{B}} T_{\mathrm{CM}} b}{\Omega_{\mathrm{q}} Q_{\mathrm{m}}}}. \tag{2.27}$$

Where b is its measurement bandwidth. Notice that high quality factors and low temperatures of the center of mass of the nanoparticle lead to high sensitivities.

Since levitated nanoparticles can be isolated avoiding dissipation, they contain high quality factors. This together with their low masses, make them ideal force sensors. Equation (2.27), stands for a general nano-resonator while in the specific case of levitated particles, the expression can be simplified as:

$$F_{\mathrm{min}} = \sqrt{4k_{\mathrm{B}}T_{\mathrm{CM}}M\Gamma_{\mathrm{CM}}b}. \tag{2.28}$$

Notice that the minimum force is proportional to the center of mass and to the damping rate Γ_{CM}, which shows that low pressures increases the sensitivity. Notice as well that if feedback cooling is applied, the effective damping rate and damping temperature must be included following the formalism given in section 2.3.3.

The equation (2.28) was deduced by implementing a direct driving scheme by Ricci [37] such that in eq (2.20) $f_{ext}(t) = \frac{F_0}{m}cos(\omega_{dr})$. The induced external force served to simulate a detectable force by the resonator.

2.7 Shortcuts to adiabaticity (STA)

As its name indicates, shortcuts are fast routes to obtain a desired result of slow physical processes. The fact that it is aforementioned as a *shortcut to adiabaticity (STA)* has to do with the particularity that the term only involves adiabatic paths when changing the parameters with which a system is controlled.

In contrast to the usual definition in thermodynamics, here the adiabatic terminology includes a broader definition. In this case any process is called adiabatic when the slow change of the control parameters of the system stay invariant to the so-called *adiabatic invariants*. They are the phase space areas in classical systems and the quantum number in quantum systems [41].

Usually STA protocols are used in isolated systems. Nevertheless, reminiscent techniques have been done in systems in contact with a thermal bath: In the case of a classical system in contact with a thermal bath, like our experiment, the realization of a STA has direct applications in the design of efficient nanothermal engines, in the driving of mesoscopic chemical or biological processes or in modifying the signal to noise ratio scheme (SNR) of sensing experiments.

2.7.1 STA in levitated nanospheres

The particular problem of our experimental setup is characterized by the Langevin equation (see section 2.4.2) where the motion of a brownian particle is driven by a white noise. In this context, the change of the control parameters of the system upset the state variables that define a particular thermodynamical state. This is the induction of a transition from one state to another of the system.

Within this framework, a shortcut can be induced in order to find a fast route to reduce the relaxation time that takes the system to thermalize from one state to another. With our current experimental setup the only time-controlled change that can be induced is the shape of the potential, but with other experimental configurations external electric/magnetic forces could also be applied from different sources.

Two standard STA methods can be applied to accelerate the equilibration in classical systems in contact with a thermal bath. On the one hand an inverse engineering and on the other hand a transposition of the counterdiabatic ideas. Nevertheless, the second provides an auxiliary potential that is not relevant from an experimental point of view [42].

The so-called engineered swift equilibration (ESE) protocols have been introduced to study the isothermal compression of a colloidal particle. Through an inverse engineering, the thermalization can be shortcutted through the compression or decompression of a harmonic oscillator from an angular frequency Ω_i to Ω_f, getting an exact scaling solution of the underdamped Fokker-Planck equation.

Protocols related to the theory of shortcuts to adiabaticity that were tested by Ignacio A. Martinez [17] in the overdamped regime need to be tested in the underdamped regime [20]. This regime can be explored by levitated nanospheres in high vacuum [15].

By implementing such protocols we would be able to control the state of a levitated nanosphere on unprecedented timescales reaching equilibrium hundreds of times faster than the natural equilibrium rate. Furthermore the realization of a shortcut has direct applications in the design of efficient nanothermal engines, in the driving of mesoscopic chemical or biological processes and in sensing experiments.

2.7.2 Engineered swift equilibration (ESE) in the underdamped regime

The ESE meethod was proposed by Ignacio A. Martínez in the reference [17] for the overdamped regime and an extension has been developed in the underdamped regime by Marie Chupeu in the reference [20]. The specific problem for a modulated potential in terms of time $U(t)$ was solved numerically by Gómez Martín [43]. Here we will resume part of the work of Chupeu with the aim of using it in the near future to pursue the first acceleration to equilibrium of a levitated nanoparticle through a time dependent potential $U(t)$.

ESE general formalism.

The probability density function $K(x, v, t)$ of an object confined in a potential and immersed in an underdamped thermal bath evolves obeying the Kramers equation:

$$\partial_t K + v\partial_x K - \frac{\partial_x U}{m}\partial_v K = \Gamma\partial_v(vK) + \Gamma\frac{k_\mathrm{B}T}{m}\partial_v^2 K. \tag{2.29}$$

Where $U(x, t)$ is the confining potential, and T the temperature of the bath. At thermal equilibrium the probability is given by the Boltzmann law:

$$K_\mathrm{eq}(x, v) = K_0 \exp\left(-\frac{U(x)}{k_\mathrm{B}T} - \frac{mv^2}{2k_\mathrm{B}T}\right). \tag{2.30}$$

By modifying the potential we can connect an initial equilibrium state with potential $U_i(x)$ and temperature T_i to final equilibrium state characterized with U_f, T_f. The ESE method assumes that the probability density function is Gaussian in the velocity variable during the change of states:

$$K(x, v, t) = \exp\left(-\mathcal{A}(x, t) - \mathcal{B}(x, t)v^2 - \mathcal{D}(x, t)v\right). \tag{2.31}$$

To keep the formalism the most general possible, the thermal bath could be time dependent. Nevertheless, we will discuss here only ESE methods with constant thermal baths since our experimental setup cannot control this variable. In the

overdamped regime this is achieved by implementing an external random function that acts as noise [44, 45] (see section 2.3.3).

The usual approach to solve equation (2.29) would be to give an input potential $U(x,t)$ and temperature $T(t)$ and obtain the solution of the probability density $K(x,v,t)$. Instead, the ESE technique adopts a reverse philosophy where the control parameters $U(x,t)$ and $T(t)$ are free and a desired dynamics is chosen for the functions $\mathcal{A}$, $\mathcal{B}$ and $\mathcal{C}$ of eq(2.31). Later, from the chosen functions, we obtain the evolution of the control parameters that can lead us to the desired dynamics.

The procedure then is to choose he functions $\mathcal{A}$, $\mathcal{B}$ and $\mathcal{C}$ and plug them in eq (2.29). The different powers of v can be separated obtaining:

$$\begin{aligned} \partial_x \mathcal{B} &= 0, \\ -\dot{\mathcal{B}} - \partial_x \mathcal{D} &= 2\Gamma \left(\tfrac{2\mathcal{B}^2 k_\mathrm{B} T}{m} - \mathcal{B} \right), \\ -\dot{\mathcal{D}} - \partial_x \mathcal{A} + 2\tfrac{\partial_x U}{m}\mathcal{B} &= \Gamma \left(-\mathcal{D} + 4\tfrac{k_\mathrm{B} T}{m}\mathcal{B}\mathcal{D} \right), \\ -\dot{A} + \tfrac{\partial_x U}{m}\mathcal{D} &= \Gamma \left(1 + \tfrac{\mathcal{D}^2 k_\mathrm{B} T}{m} - \tfrac{2\mathcal{B} k_\mathrm{B} T}{m} \right). \end{aligned} \tag{2.32}$$

These sets of equations must hold in order to connect the two imposed states. Of course, they have to be adapted to specific protocols with desired constraints, such as duration of the protocol, amplitude of the transition and number and nature of control parameters.

Time-modulated potential protocol

In our specific case, the potential will not be position-dependent and therefore large simplifications can be done. A variant of this problem was solved numerically by Gómez Marín [43]. Furthermore in our case the temperature will be constant.

The parameter from the potential that is changed from the power is the stiffness (see eq 2.5) giving therefore a certain trap frequency $\Omega(t)$, we define the time-dependent potential as:

$$U(t,x) = \frac{m\Omega^2(t)}{2} x^2. \tag{2.33}$$

And the temperature we set it constant. Under these conditions the probability density is now written in a simplified form:

$$K(x,v,t) = N(t) \exp\left(-\alpha(t)x^2 - \beta(t)v^2 - \delta(t)xv \right). \tag{2.34}$$

Where for analogy $\mathcal{A}(x,t) = \alpha(t)x^2 - \ln N$, where $N(t)$ normalizes the function, $\mathcal{B}(x,t) = \beta(t)$, and $\mathcal{D}(x,t) = \delta(t)x$. The equations (2.32) are then simplified as:

$$\begin{aligned} -\dot{\alpha} + \Omega^2 \delta &= \tfrac{\Gamma k_\mathrm{B} T}{m}\delta^2, \\ -\dot{\beta} - \delta &= -2\Gamma\beta + 4\tfrac{\Gamma k_\mathrm{B} T}{m}\beta^2, \\ -\dot{\delta} - 2\alpha + 2\Omega^2\beta &= -\Gamma\delta + 4\tfrac{\Gamma k_\mathrm{B} T}{m}\beta\delta. \end{aligned} \tag{2.35}$$

With boundary conditions that correspond to the initial and final state:

$$\begin{gathered}\alpha(0)=\frac{m\Omega_i^2}{2k_{\mathrm{B}}T_i},\quad \alpha\left(t_f\right)=\frac{m\Omega_f^2}{2k_{\mathrm{B}}T_f},\\ \beta(0)=\frac{m}{2k_{\mathrm{B}}T_i},\quad \beta\left(t_f\right)=\frac{m}{2k_{\mathrm{B}}T_f},\\ \delta(0)=\delta\left(t_f\right)=0.\end{gathered}\tag{2.36}$$

In the next steps Chapeau simplifies the equations, re-scaling them and defining a new time variable $s=\frac{t}{t_f}$. Then, from now on the dot refers to derivatives with respect to the re-scaled time , where t_f is the time at which the modulated function stops running.

$$\begin{aligned}\dot{\widetilde{\alpha}}&=2N_\Omega\tilde{r}\tilde{\delta}-2N_\Gamma\widetilde{\delta}^2,\\ \dot{\widetilde{\beta}}&=-2N_\Omega\tilde{\delta}+2N_\Gamma\widetilde{\beta}-2N_\Gamma\widetilde{\beta}^2,\\ \dot{\tilde{\delta}}&=-N_\Omega\widetilde{\alpha}+N_\Omega\widetilde{\kappa}\widetilde{\beta}+N_\Gamma\tilde{\delta}-2N_\Gamma\widetilde{\beta}\tilde{\delta}.\end{aligned}\tag{2.37}$$

such that:

$$\widetilde{\alpha}\equiv\frac{2k_{\mathrm{B}}T_i}{m\Omega_i^2}\alpha,\quad \widetilde{\beta}\equiv\frac{2k_{\mathrm{B}}T_i}{m}\beta,\quad \tilde{\delta}\equiv\frac{k_{\mathrm{B}}T_i}{m\Omega_i}\delta,\quad \widetilde{\Omega}\equiv\frac{\Omega}{\Omega_i},\quad \widetilde{\kappa}\equiv\frac{\kappa}{\kappa_i}=\widetilde{\Omega}^2.\tag{2.38}$$

Where $N_\Gamma=\Gamma t_f$ and $N_\Omega=\Omega_i t_f$ are two introduced parameters that are key to understand the possible protocols.
The chosen selected conditions:

$$\begin{gathered}\widetilde{\alpha}(0)=1,\quad \widetilde{\alpha}(1)=\left(\frac{\Omega_f}{\Omega_i}\right)^2=\chi,\\ \widetilde{\beta}(0)=\widetilde{\beta}(1)=1,\\ \widetilde{\delta}(0)=\widetilde{\delta}(1)=0.\end{gathered}\tag{2.39}$$

After some more definitions Chapeau arrives to the following final differential equations that play a key role in finding the functions of the stiffness:
He defines:

$$\widetilde{a}=\frac{2k_{\mathrm{B}}T_i}{m\Omega_i^2}a=\widetilde{\alpha}-\frac{\widetilde{\delta}^2}{\widetilde{\beta}}.\tag{2.40}$$

And

$$\widetilde{\Delta}=\tilde{a}\widetilde{\beta}.\tag{2.41}$$

Obtaining:

$$\widetilde{\beta}=1-\frac{\tilde{\Delta}}{2N_\Gamma\widetilde{\Delta}}.\tag{2.42}$$

$$\tilde{\delta}=\frac{\widetilde{\beta}\dot{a}}{2N_\Omega\tilde{a}}.\tag{2.43}$$

And as a final equation for the stiffness:

$$\widetilde{\kappa}=\frac{\dot{\alpha}}{2N_\Omega\delta}+\frac{N_\Gamma}{N_\Omega}\delta.\tag{2.44}$$

Although the process seems tedious it leaves a very simple method to compute possible solutions of the stiffness. He refers to two possible protocols in order to compute

such frequency:

Protocol A: Choose shape of $\widetilde{\Delta}(s)$, deduce then $\tilde{\beta}$ from eq(2.42), then compute $\tilde{a}$ from eq (2.41), then $\tilde{\delta}$ follows from eq(2.43) and finally the stiffness in computed from eq(2.44)

Another route towards an explicit protocol consists in choosing the function $\beta(\tilde{s})$ and deduce the other functions from it. Nevertheless, Chapeau finds that, after some analytic steps, this method requires numerical methods.

2.7.3 Relaxation times and ESE possible protocols.

Two time-scales are key to understand the possible protocols. On the one hand the time period of the oscillation $1/\Omega$ and on the other hand the time associated with the friction $1/\Gamma$. This scales are compared to the duration of the protocol t_f through the previous introduced parameters $N_\Gamma = \Gamma t_f$ and $N_\Omega = \Omega_i t_f$. From there the timescale of position relaxation is defined as $t_x = \Gamma/\Omega_i^2$ and the timescale of the velocity or momentum relaxation as $t_v = 1/\Gamma$. Nevertheless, for units consistency in the later discussion of the results we use the regular damping coeffitient to define the momentum relaxation time since it is expressed in seconds. The relation of these times is $\tau_p = 2\pi t_v = 2\pi/\Gamma$.

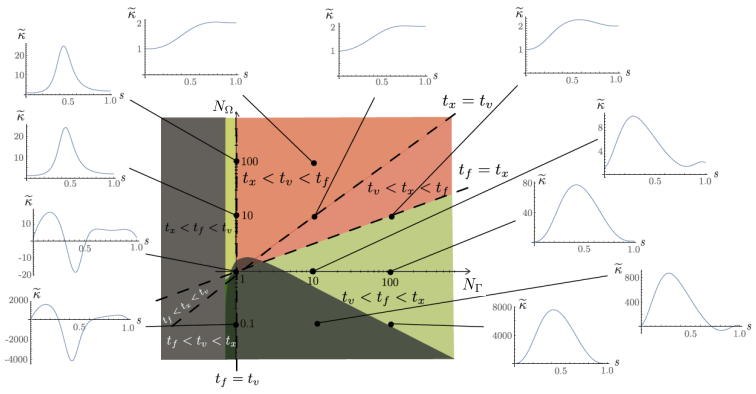

Figure 2.3: Behaviour of the stiffness during the compression protocol. The diagram shows different possibilities of the stiffness for three compared time parameters: the duration of the protocol t_f, the angular position relaxation time t_x and the angular velocity relaxation time t_v. They are compared through the parameters $N_\Gamma = \Gamma t_f$ and $N_\Omega = \Omega_i t_f$. The colors indicate zones classified in terms of the capability to accelerate of the protocol. Red zones show slow protocols (t_f is the largest) and therefore less interesting. The green ones show interesting protocols for a relaxation shortcut. Finally grey areas show negative stiffness areas which are not possible to do experimentally. Remember that $s = t/t_f$ and the time axis of the evolution of the stiffness is therefore normalized. Obtained from reference [20].

Note that the maximum of these last two timescales defines the global relaxation timescale of the system. For our system the momentum relaxation is longer and therefore this is setted as the relaxation time of the system $\tau = \tau_p$.

With these definitions possible protocols can be checked in figure 2.3. Green areas show compression protocols that would allow the acceleration of the system. For our frequency $\Omega \approx 100$ kHz, we have that $t_v > t_x$ and therefore we are interested in protocols where $t_s < t_v < t_x$ which corresponds to the stretched green region for $N_\Gamma < 1$ and $N_\Omega > 1$.

2.8 Heat engines

STA can help us improve the efficiency of nanothermal engines optimising their design [41]. Ignacio A. Martinez explored stochastic heat engines in the overdamped regime [28] developing together with J.M.R. Parrondo a Carnot engine [29] .There are theoretical proposals for the underdamped regime that are of interest to be tested with levitated nanospheres [26, 27].

Shorcut methods used with colloidal particles implement non-trivial functions to an input parameter (usually optical potential stiffness) of the equation of motion in order to optimize a process. These functions are usually found through the so-called *reversed philosophy* where instead of solving the equations of motion as usual (inputs i.e. stiffness give outputs i.e. position distributions), an imposed and desired solution of the equation gives back only certain possibilities of possible input parameters of the potential stiffness. In the case of speeding-up relaxation processes the non-trivial input function is implemented in the stiffness and is found such that the relaxation is shorcuted as much as possible [17]. Nevertheless, in the design of efficient heat engines the input function is found such that the adiabatic processes of a full cycle give maximum efficiency [26, 27].

A colloidal stochastic heat engine converts heat flow into mechanical work operating under a cyclic process. The cycle contains two isothermal processes where there is a variation of the potential to extract or implement work and two adiabatic processes with an instantaneous reduction/increase in temperature, see figure 1. Compression and expansion are achieved by increasing and decreasing the potential of the harmonic potential that traps the nanospheres, while heating and cooling is done by changing the effective temperature of the center of motion particle.

While the overdamped regime has been well explored, the underdamped regime lacks experimental results. It is of interest to check optimal protocols for maximum efficiency at fixed power. Can we determine optimal driving protocols for different values of power? Could we extend the results to include feedback control? Can we explore the quantum regime at high vacuum and attain Carnot efficiencies? [30]

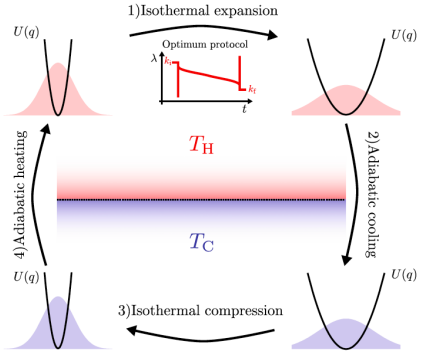

Figure 2.4: Stochastic heat engine cycle. Obtained from reference [11]

Additionally the realization of a shortcut can modify the signal to noise ratio (SNR) scheme helping to improve sensing tests of a certain frequency. When a STA process is implemented within a time shorter than a specific resonance, it leads to the transitory cancellation of the resonance signal [18]. It is a transitory process due to the equipartition theorem. The shortcut causes an energy transition from the selected resonance to the rest of modes and degrees of freedom of the system. In our particular case currently we detect three degrees of freedom related to center of mass motion along the 3 directions in which the nanosphere can move. Therefore a short-cut would cause an energy transition from one selected degree of freedom to another. Nevertheless, additional degrees of freedom can be found in particles with anisotropic geometry, which polarizabilities (described by a tensor) change with the polarization vector of the light field. In the case of, for instance, a nanodumbell the linear, circular or elliptical polarization, can inject rotation, torsion or a combination of both respectively on the trapped object [21, 22].

By monitoring the dynamics of a colloidal particle while implementing cycles of a heat engine, one can extract the work statistics. A stochastic heat engine converts heat flow into mechanical work operating under a cyclic process. To apply work to a nanoparticle we could either modulate the optical potential or implement an external force through a control parameter $\lambda(t)$ such that the time variable of the potential or external force are changed as $U(q, \lambda(t)); \quad f(q, \lambda(t))$. For example for a harmonic potential $U(q,t) = \mathrm{k}(t)q(t)^2/2$, the control parameter is $\lambda(t) \equiv \mathrm{k}(t)$, but another possibility would be to implement a ratchet moving the trap and being its center then, the control parameter. Nevertheless, for the general case we will consider $\lambda(t)$.
Implementing both, an external force and a modulated potential, the incremented work and heat reads as:

$$\mathrm{d}\mathcal{W} = (\partial U/\partial \lambda_c)\,\mathrm{d}\lambda_c + f\ \mathrm{d}q, \tag{2.45}$$

$$\mathrm{d}\mathcal{Q} = F\ \mathrm{d}q. \tag{2.46}$$

Where $F\,(q, \lambda_c) = -(\partial U)/(\partial q) + f$ is the total force acting on the particle with the contribution of the external force f and the modulated potential. If the external force

has both deterministic and stochastic contributions, then along a long trajectory:

$$\begin{aligned} \mathcal{W}(q(t)) &= \int_0^\tau \left[(\partial U/\partial \lambda_c)\, \dot{\lambda}_c + f\dot{q} \right] \mathrm{d}t, \\ \mathcal{Q}(q(t)) &= \int_0^\tau \dot{\mathcal{Q}} \mathrm{d}t = \int_0^\tau F\dot{q}\ \mathrm{d}t. \end{aligned} \tag{2.47}$$

Consider now that the only external implementation is the modulation of the potential such that $U(q,t) = \mathrm{k}(t)q(t)^2/2$ and taking its stiffness as the control parameter. Then for expansions processes when the stiffness of the trapped potential is decreased, it is usually convenient to consider the equations of motion of the mean square displacement or variance:

$$\dot{\sigma}_q^2 = -m\mu\ddot{\sigma}_q^2 - 2\mu\mathrm{k}(t)\sigma_q^2 + 2m\mu\sigma_v^2. \tag{2.48}$$

where $\mu = 1/\left(m\Gamma_{\mathrm{CM}}\right), \sigma_n^2(t) \equiv \langle \dot{q}^2(t) \rangle$. At this point the usual approach for colloidal particles is to simplify equation (2.48)neglecting the term proportional to $\ddot{\sigma}_q^2$ since in the overdamped regime $\Gamma_{\mathrm{CM}} >> \Omega$. This simplification in the overdamped regime allows to deduce analytically protocols of the evolution of λ_c that maximize the efficiency of a stochastic heat engine. There is not known analytic solution of protocols in the underdamped case, instead numerical methods are used. Very rapid variations of the the control parameter are necessary for optimum protocols in both regimes, a particle reacts slowly to variations of the control parameter in the overdamped regime and fast in the underdamped regime. Therefore it must be more optimum to extract work with in the underdamped regime.

Chapter 3

Methods

This chapter describes first the scheme of the current and future planned experimental setups. Second it presents the new implemented devices during this academic year: a picoscope, an electric optical modulator (EOM) and a wave generator. We explain some of their important characteristics to take into account when performing experiments. Third, we give the steps and methodology taken in the experiments during this master project. Finally an important effort has been devoted to the calibration process to transform the recorded signal into position, as well as a discussion of its errors and possible improvements in section 3.3.

3.1 Experimental setup

First we will present the setup with which we measured the results shown in this master project. Notice that the current setup includes the feedback mechanism and a photodetector to measure the longitudinal direction of the particle.

In fig 3.1 we can find the current experimental setup which we describe here.

In the first compartment the source of a Mephisto MOPA laser produces a gaussian profile beam in the transverse electromagnetic mode TEM00 and at a wavelength of 1064nm. We use a power amplifier at a fixed current of 54A (nevertheless, in appendix C the current is slightly changed to observe modifications of the FFT).

The beam is redirected to the second compartment with a round wedge prism where a galilean telescope (GT) adjusts the size of the beam in order to focus it through the EOM. Before entering it, a half wave plate (HWP) sets an horizontal polarization of the beam. The EOM varies the polarization through time since a voltage function is applied with a function generator changing the polarizability properties of the crystal through which the laser light travels (see section 3.1.1). The modified laser enters then a polarization-maintaining fiber (PMF).

The laser gets out of the second compartment through the PMF and is directed with mirrors to the polarization beam splitter which allows for passing only hori-

zontally polarized light into the vacuum chamber. Since the EOM is changing the polarization through time and the HWP only allows horizontally polarized light to pass, this results in a power modulation. This effect is double checked with another HWP after the PBS that is also setted to only allow horizontal light to pass. (For the appendix C we analyze the effects of changing the polarization with this HWP).

The laser is focused with a microscope objective (MO) of numerical aperture NA=0.8 creating a high intensity gradient of the laser that sets the optical trap. We can check wether a particle is trapped with a CCD camera that is focused to the center of the trapped from outside the vacuum chamber. Once a particle is trapped after nubelizing (see section 3.2.2), the scattered light is collected with an aspheric lens collimating it out of the vacuum chamber. Finally the beam enters the detection

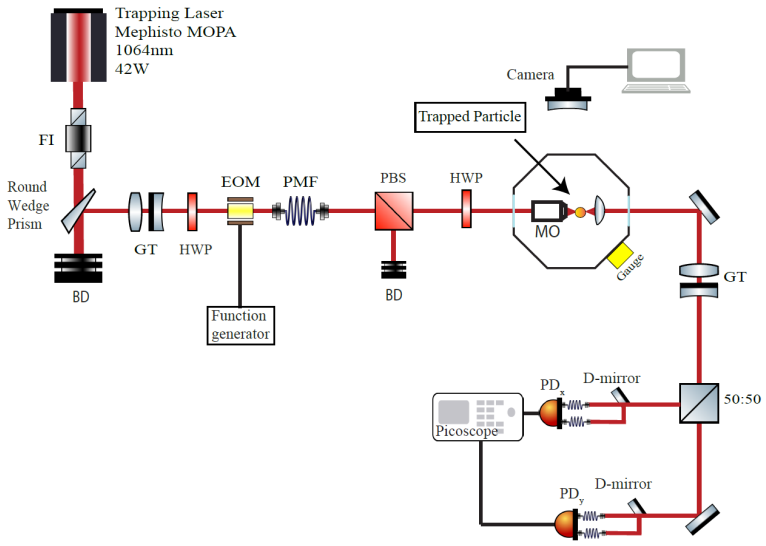

Figure 3.1: Simplified scheme of the experimental setup.

system where the beam is splitted 50:50 in order to detect the vertical y and horizontal x motion modes of the particle. We use the method of differential detection where by using D-shaped mirrors the horizontal signal is divided into right and left components, and the vertical signal into top and bottom components. These signals are then detected using photodiodes (PD) and collected with multimode fibers to the amplifiers. There, the difference between the splited components of each orientation is measured and the result amplified by a factor of 10^6. Finally we record the signals in the picoscope.

3.1.1 Picoscope, wave generator and EOM.

Picoscope

A Picoscope 5000 series reads the recorded signal of the photodiodes as well as the generated wave from the function generator. A picoscope 5000 series have certain limitations such as the sampling rate and amount of data samples saved per time. The inputs to record a signal are the collection time, the amount of samples and the number of bits. For the selected inputs it gives a certain sampling rate according to its limitations. The limitations of the samplin rate and amount of collected data per time change depending on the number of channels used and the bits. One can find the details in the manual.

Figure 3.2: Picoscope.

All the experiments are done by using the same channels for specific signals. We use channels B and C to read the difference of the horizontal and vertical modes respectively. Channel D is used for the generated signal and finally in channel A we record one of the not-substracted signals of the two photodiodes.

Wave generator

A wave generator Rigol DG1032Z supplies a recorded signal to the EOM. It is a 2 channel Function / Arbitrary Waveform Generator to create high quality signals up to 30 MHz (Sine) with very low jitter (200 ps) and the new SiFi (SIgnal FIdelity) technology. The device includes an USB-Host- and an USB-device interface which allows to program your own functions. This is of use in order to pursue a shortcut so we can implement certain desired functions. Nevertheless, for the thesis we use

a square wave. Usually this signal is amplified by a factor of 40 before arriving the EOM that has a half-wave voltage of 330V.

Figure 3.3: Function generator.

Electric optical modulator EOM

An electric-optical amplitude modulator SN U00885 RF IN is used in order to modulate the polarization through time and with the help of a half wave plate before the laser enters the EOM and another one afterwards, we modulate the intensity.

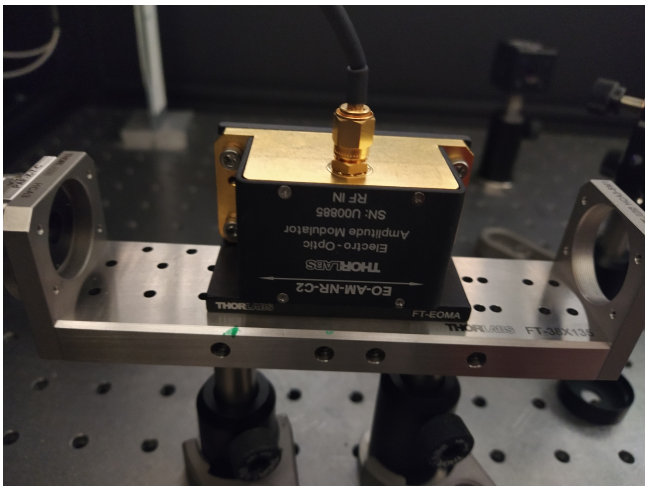

Figure 3.4: EO Amplitude Modulator SN U00885 RF IN.

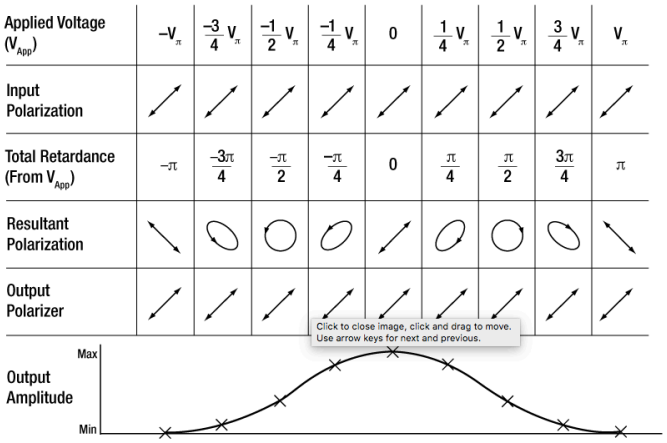

Figure 3.5: EO Amplitude Modulator output as a Function of Applied Voltage (Listed in Terms of V_π

With the EOM and the help of a polarizer we can reduce the electric field amplitude at the rate of the applied voltage to the EOM. And the nanosphere potential stiffness is proportional to the square of the amplitude. . In order to change double the stiffness we need to change a root-square of 2 the amplitude. Roughly speaking, the initial amplitude of the electric field must equal 0.7 the final amplitude. From figure 3.5, this requires roughly a voltage of $1/4V_\pi$ which is aprox $80V$ since at our wavelength ($1064nm$) the Half-wave voltage (V_π) of the EOM is around 330 V.

The physical principle of the EOM is the following. Applying $V_\pi = 330V$ to the EOM we change 90 degrees the polarization. With the help of a polarizer it would be translated as a zero output amplitude (see fig 3.5). With the same logic applying to the EOM a voltage of 165 V, we would reduce by half the output amplitude. Notice that by changing the offset

At the moment we are able to generate with a function generator a signal of a maximum amplitude of 10 volts. This signal is amplified 20 times applying to the EOM a signal of 200 V amplitude. Nevertheless, with the help of an offset we could reach the Half-wave voltage required to change 90 degrees the polarization (which is not needed for our purposes).

We need to set an offset to this wave. Otherwise we do not change the output amplitude since same values of positive and negative voltage would apply the same polarization contribution to the output light (see fig 3.5). Since we apply a square wave to the EOM, without offset we do not change the output amplitude. This is because a square wave generates same positive and negative values of voltage. The EOM therefore would change the same amount but in different directions the polarization. And when the light passes through the output polarizer both lights with different polarizations would contribute the same amount after the output polarizer. Since we need a change of about 80 V and also an offset, a wave of 40 V amplitude

and the same value of offset would fit our estimations.

Choice of parameters

In order to observe the relaxation process of the nanosphere we need to set very specific values to the wave generator and to the picoscope. Find the table below where we organise the choice of values:

Pressure (mbar)	Relaxation time (ms)	Frequency of square wave (kHz)	Picoscope collection time (amount of data stored)	Picoscope samples
10 mbar	≈ 0.03 ms	10 kHz	100 ms/ div	10MS

Table 3.1: Choice of parameters for the expected relaxation time.

Let us explain here how we made this choice:

1. The frequency of square wave is chosen to be able to observe the relaxation of the particle. A choice of 10 kHz allows to look for compression/decompression cycles of 0.05 ms which is slightly longer than the relaxation time therefore observing the appropriate time-scale.

2. Picoscope collection time. With this option in the picoscope we select for how long we store data. The scope always shows 10 divisions and stores until the last time value of the 10th division. For instance the option of 100 ms/div would store 1 second of data. The longer, the more cycles of the process we measure but it is more appropriate to store different fields since otherwise the picoscope would limit the sampling rate, and the higher the sampling rate the better the resolution. For instance for a square wave of period 1ms, if we measure during 10^4 ms we would get 10^4 cycles. The scope always shows 10 divisions and stores until the last time value of the 10th division.

3. Picoscope sampling rate. We need to select how many samples we store per second. To answer this question we first should decide how many samples per jump/cycle we want to store. For instance if we decide to have 10^4 samples per jump, for a wave frequency of period 1ms we need 10MS/s while for a wave of period 10 ms we need 1 MS/s. It is nevertheless usually convenient to maximize this parameter doing appropriate choice of number of samples and collection time (see the manual for limitations).

4. Amplitude of square wave. We would like to double the stiffness of the optical potential. Amplitude of 10 V is enough due to the steps discussed in the section 3.1.1.

3.2 Methodology

In this section we will explain the steps taken when performing the experiments to obtain the results shown in this master project.

3.2.1 Power monitorization

Ideally, before trapping the nanoparticles, a measurement of the laser power before the macroscopic objective helps us to keep track on its fluctuations through time. It also help us to analyze what values of the laser power improve the likeness to trap for long times and when the trapping is stable while going to low pressures. From my experience usually higher powers close to 4.5 mW while using the OD2 filter lead to a better stability but with values close to 3.5mW is easier to trap at the beginning. This could be explained since higher powers lead to deeper trapping potentials.

Figure 3.6: Power meter.

3.2.2 Particle loading

To load the trap we fill an OMRON MicroAir U22 nebulizer (see figure 3.7) with a solution that contains 50 mg of silica particles of 143 nm diameter and density of 1.85 g/cm3 with 1 ml of ethanol. The nubelizer contains a piezoelectric crystal that vibrates at frequencies around $1-3$ MHz to generate a fountain of gas through the Bernoulli principle. The piezoelectric shakes the solution increasing its kinetic energy with a simultaneous decrease in its potential energy which includes static pressure and internal energy causing its vaporization.

Figure 3.7: OMRON MicroAir U22 nubelizer.

The nubelizer is used to vaporise the solution inside the vacuum chamber through a funnel. This allows to spread the vapor in a localized region. By moving the funnel very carefully and with the help of the CCD camera that detects the scattered light of the laser, we select to vaporize in the region closest to the focus of the laser beam. Afterwards it is of help to close the vacuum chamber before the particle gets trapped. This is in order to avoid the instability that an external air current might induce on the system as well as to avoid any vibration that we might induce while closing the chamber.

The CCD camera allows us to detect the trapping of particle/s inside the optical trap. The brightness of the detected particle is not always the same indicating that the scattered light also changes. This could be related to thermal fluctuations of the laser. In some occasions we also trap more than one particle or bigger particles since while vacuuming, the frequencies are not shown at the expected values in the fourier transformed detected signal.

3.2.3 Towards vacuum

Once the vacuum chamber is closed (see fig 3.8), and we trapped a stable particle, we slowly open the vacuum valve in order to go to low pressures. The reason why slow opening is necessary is to not induce high air currents on the system that might cause instability and loss of the trapped particle. Lowing the pressure from atmospheric to 10 mbar might take between 1 and 3 hours in the present.

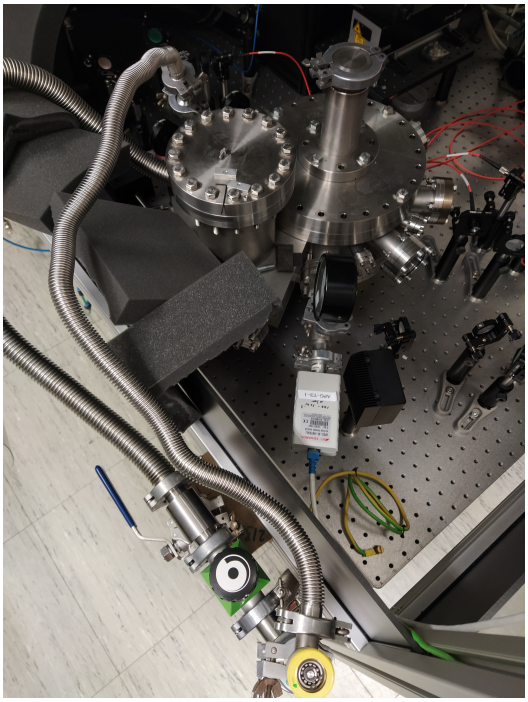

Figure 3.8: Vacuum system. Vacuum chamber and three valves: Yellow wheel-shape valve is opened first and allows to get down to pressures of the order of 1mbar. The black wheel-shape valve allows to reduce the pressure up to 10^{-3} mbar. Finally the blue L-shaped valve is used to get the system back to atmospheric pressures when the others are closed. The valves are all connected with tubes to a mechanical pump. Foam protections are used to avoid vibrations that can cause instability on the system while opening the valves. In the future a turbo-pump might be implemented to get to lower pressures with high control.

3.2.4 Signal allignment and data acquisition

While we open the valve we must make sure to get enough power to the photodiodes and that the alignment is correct. In fig 3.9 we represented visually how the collected light of the laser is losing power through its path in order to record the 3 different directions.

We must be sure that each photodiode gets the very same power and read therefore similar values of the voltage. See in fig 3.9 that once the scattered light is collected with an aspheric lens and collimated, a fraction of the power is deviated in order to record the longitudinal position. With the use of a power meter we make sure that this is only a third of the total collected power. The 2/3 of the remaining power

is directed with mirrors and again once must make sure to split these ramining power 50:50 for measuring the vertical and horizontal motion modes. To do this we play with the mirrors. Later we use the photodiodes wheel holders in order to align the laser. A usual resource is to connect a visual laser to the input of the multimode-fiber. Nevertheless, usually this is not necessary.

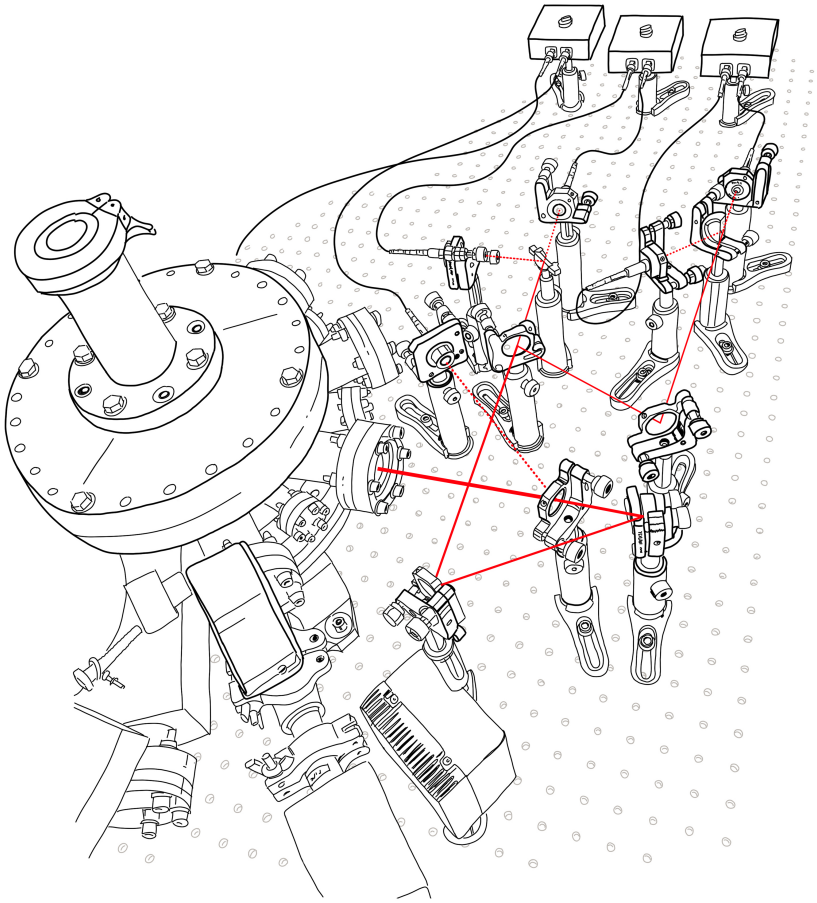

Figure 3.9: Detection system.

Once we have signal inside a photodiode we try to maximise it and equally share it witthin both of the photodiodes of the same mode. Once the power is equal, the difference of both must be zero. Usually during the experiment we need to repeat this step several times sine the laser often suffers small misalignments that could be related to temperature variations of the source or small changes on the holders of the mirrors that guide the laser.

3.3 Calibration

The scattered light of a nanoparticle is collected by an aspheric lens. Its power is given by:

$$P_{\text{scat}} = |\alpha|^2 k_{\text{L}}^4 I_{\text{opt}} / 6\pi\epsilon_0^2. \tag{3.1}$$

Notice that the scattered power light depends on the local intensity I_{opt} and is therefore changing as the particle moves inside the potential well. This allows for position sensitivity via calibration. It also depends on the wavevector k_{L} and the polarizability α. The polarizability depends on the radius (see eq(2.2)), and therefore the scattered light that one can detect rapidly increases with the radius.

The detection is done with a photodetector that converts the injected photons in voltage. The detected signal measured in voltage must therefore be calibrated and converted into position. This is a big source of uncertainty in most of the experiments.

The standard method is to fit the recorded data to the expected PSD or the variance of the position distribution. This method nevertheless, has around a 30 % uncertainty [10, 46] for various reasons: It assumes the particle is in equilibrium and we already discussed that if a modulation in terms of time is implemented on the particle non-equilibrium behavior must be considered. The method also assumes that the motion can be treated as a harmonic oscillator since eq (2.17) is used to fit the data and the potential is not always harmonic [36], but this can be compensated [46]. Furthermore, the method requires the knowledge of the local temperature near the particle and the mass of the particle. The temperature is not always measured with accuracy and the mass can be calculated from measuring the damping rate, but this requires accurate knowledge of the particle shape and density. Finally it has been shown that calibration is pressure dependent [46].

Another possibility is to use an external force in order to calibrate a detector. For instance an electric force [46, 47], but this requires a good knowledge of the external applied force. It is also possible to use a measurement of combined frequencies to extract the damping, with high precision [48].

In this thesis we will follow the linear-calibration approach fitting the PSD and we will analyze its errors. Future corrections to this model could be done taking into account non-linearities of the trapping potential or using a harmonic driving force [46].

3.3.1 Calibration for harmonic trapping potential

There are two equivalent ways to calibrate the detector for a harmonic brownian particle in thermal equilibrium. They both assume that the photodiode signal V_i at a certain direction $i = x, y, z$ is proportional to the corresponding particle displace-

ment q_i via the calibration factor:

$$c_i = V_i/q_i. \tag{3.2}$$

1. The first method consist of calculating the variance of the recorded voltage time trace $V_i(t)$ and use the equipartition theorem, which states that the averaged potential energy is given by:

$$\langle E_{\rm pot}\rangle = \frac{1}{2}m\Omega_0^2\langle q^2\rangle = \frac{1}{2}m\Omega_0^2\frac{\langle V^2\rangle}{c_{\rm calib}^2} = \frac{1}{2}k_{\rm B}T_b\ . \tag{3.3}$$

The use of the mass m, the bath temperature T_b and the oscillation frequency Ω_0 is necessary to obtatin c_i from eq (3.3). For higher pressures than $1mbar$ it can be assumed that the bath temperature equals the temperature of the vacuum chamber which can be measured with a thermometer. The oscillation frequency Ω_0 can be obtained from the PSD of the experimental data. Finally the mass can be obtained from the size and density provided by the manufacturer, but this assumption may introduce an error as the particle size is not perfectly monodisperse. Instead, an independent calibration of the particle mass can be done fitting the PSD.

2. We used the following method in which we obtain the experimental spectral density of the voltage signal $S_{VV}(\Omega) = c_{\rm calib}^2\, S_{qq}(\Omega)$ and we fit it to eq (2.17). This method is equivalent to the previous one since the deduction of equation (2.17) makes use of the equipartition theorem as well, (see the derivation of eq(2.17) in the ref [49]). Nevertheless, it only requires one fit since the mass can also obtained from it, being therefore more accurate a priori. We explain it here below.

Using the PSD for calibration

a) Obtain the two-sided PSD $S_{VV}(\Omega)$ of the recorded $V(t)$. Due to the noise from the driving stochastic function $\Xi(t)$ averaging many experimental PSD S_k^{rec} will give a closer result to the expected formula given by the eq (2.17):

$$S(\Omega)_{qq} \equiv <S_k^{rec}> \approx |\chi(\Omega)|^2 S_{\rm ff}(\Omega) = \frac{\Gamma_{\rm CM}{\rm k_B}T_{\rm CM}/\pi m}{\left(\Omega^2-\Omega_0^2\right)^2+\Gamma_{\rm CM}^2\Omega^2}. \tag{3.4}$$

In our case we use the Welch's average periodogram method [50] to compute such PSD through data compression by windowing techniques. A different way to reduce the noise in a recorded spectrum is "blocking". A block of consecutive data points $\left(\Omega_{k_1}, S_{k_1}^{rec}\right)\ldots\left(\Omega_{k_2}, S_{k_2}^{rec}\right)$, are represented by only one new data point $\left(\overline{\Omega_k}, \overline{S_k^{rec}}\right)$, [51]. We briefly discuss the different techniques at the end of this section.

b) Rewrite eq (2.17) into eq (3.5) with $S_{VV}(\Omega) = c_{\rm calib}^2\, S_{qq}(\Omega)$ and by setting $A = c^2\langle q^2\rangle = c^2\frac{k_B T_{\rm CM}}{m\Omega_0}$; $\Omega = 2\pi f$; $\Omega_0 = 2\pi f_0$; $\Gamma = 2\pi g$, and fit it to the experimental data with free parameters A, f_0 and g.

$$S_{VV}(f) = \frac{A}{4\pi^2}\frac{2f_0^2 g}{\left(f^2-f_0^2\right)^2+f^2g^2}. \tag{3.5}$$

We use *lmfit* from Python using techniques reminiscent to least-squares fitting. Notice that one must be consistent and if one prefers to use the one-sided PSD $\hat{S}(f)$ the following change must be done $\hat{S}(f) = 4\pi S(\Omega \geq 0)$ [46].

c) Obtain the particle radius from eq(3.6) and the mass from the density ρ_{part} and the volume computed with the obtained radius R and assuming an spherical particle:

$$R = 0.619 \frac{9}{\sqrt{2\pi}\rho_{\text{part}}} \sqrt{\frac{M}{N_{\text{A}} k_{\text{B}} T}} \frac{P_{\text{gas}}}{\Gamma_{\text{gas}}}. \tag{3.6}$$

Here M is the molar mass of the gas.

d) Obtain the calibration factor from the definition of A as $c = \sqrt{Am\Omega_0^2 / (k_{\text{B}} T)}$.

Least-squares fitting assumes first that the data points follow a Gaussian distribution and second that they are statistically independent. Since the first condition is usually not fulfilled, data compression is necessary in order to obtain a not-noisy data set that is normally distributed. When using data compression by windowing with a large number of windows, the values of the compressed power spectrum become statistically independent and Gaussian distributed fullfilling the above-exposed conditions. While windowing compresses to equidistant points on the frequency axis, blocking does not have this constraint, and is therefore useful for data display with the logarithmic frequency axis. A free MATLAB code that they developed to calibrate optical tweezers with this technique can be found in ref [52].

Systematic calibration errors.

The calibration model implemented here contains errors related to the pre-made assumptions that could be corrected with better models as discussed at the beginning of this section. But it also contains systematic errors related to the measurement devices, or missing information of the material parameters. To estimate the error of the calibration, we consider that $c^2 = Am\Omega_0^2 / (k_{\text{B}} T)$ performing error propagation:

$$\frac{\sigma_{c^2}^2}{(c^2)^2} = \frac{\sigma_A^2}{A^2} + \frac{\sigma_m^2}{m^2} + 2^2 \frac{\sigma_{f_0}^2}{f_0^2} + \frac{\sigma_T^2}{T^2}. \tag{3.7}$$

For the errors σ_A and σ_{f_0} we use the uncertainties obtained from the fitting using the least square method.

The standard deviation of the mass σ_m comes from $m = 4\pi\rho_{\text{part}} R^3/3$ and using eq (3.6):

$$\frac{\sigma_m^2}{m^2} = \frac{3^2\sigma_g^2}{g^2} + \frac{\left(\frac{3}{2}\right)^2 \sigma_T^2}{T^2} + \frac{3^2\sigma_{p_{\text{gas}}}^2}{{p_{\text{gas}}}^2} + \frac{2^2\sigma_{\rho_{\text{part}}}^2}{\rho_{\text{part}}^2} + \frac{\left(\frac{3}{2}\right)^2 \sigma_M^2}{M^2}. \tag{3.8}$$

Here the error from the damping term can also be used from the uncertainty of the fitting. The temperature error requires a measurement of the temperature inside the vacuum chamber which is still not performed and is therefore taken equal to

10%. The error of the gauge pressure is of 10%, the density of the particle of 5% and the molar mass as well [46]. Finally the calibration error is computed through:

$$\sigma_c^2/c^2 = \sigma_{c^2}^2/\left[4\left(c^2\right)^2\right]. \tag{3.9}$$

Obtaining an error of more than 30%, see section 4.1.1.

Energy calibration.

For many applications it is usually sufficient to know the energy of the oscillation mode. In this case it is possible to define a calibration factor that does not contain the uncertainties of the mass error:

$$C = \frac{c^2}{m} = \frac{\Omega_0^2 \langle V^2 \rangle}{k_{\mathrm{B}} T}. \tag{3.10}$$

Since fitting errors are usually small, the uncertainty of this calibration factor is now mainly limited by the uncertainty of the temperature measurement. It can be calculated from $C = A\Omega_0^2/\left(k_{\mathrm{B}} T\right)$.

Notice that the energy of a harmonic brownian particle is given by:

$$E(x,p) = \frac{1}{2} m\Omega_0^2 x^2 + \frac{p^2}{2m} = \frac{1}{2} m\Omega_0^2 \bar{x}(t)^2. \tag{3.11}$$

Where the second equality follows from the slowly varying amplitude approximation $x(t) = \bar{x}\sin\left(\Omega_0 t\right), \dot{\bar{x}} \ll \Omega_0 \bar{x}$ which is fulfilled if the amplitude takes many oscillation periods to change. In literature usually an analysis of $\frac{E}{k_B T}$ is done [15].

Notice from eq(3.3) that therefore the potential energy can be calculated as:

$$E_p = \frac{1}{C} \frac{\Omega_0^2 \langle V^2 \rangle}{k_{\mathrm{B}} T}. \tag{3.12}$$

And the same can be done for the total energy in cases where the slowly varying amplitude approximation is fulfilled.

Chapter 4

Experimental results

This chapter is divided in two sections:

In the first one we monitor the position and velocity of a levitated nanosphere at a pressure of 9 mbar and at timescales shorter than its relaxation time observing ballistic brownian motion. We obtain its MSD and the expected relaxation time.

In the second section we present an experiment where by changing the intensity of the laser among two values we create two different equilibrium states. We study the transitory dynamics of compression and decompression cycles. The nanoparticle at equilibrium in the first state is compressed/decompressed to the second and its dynamics are studied at time-scales of the order of the relaxation time and at a similar pressure of 10 mbar. During the compression processes, the stiffness of the optical potential is changed from the first state to the second with a step function such that $k_f = 1.8k_i$. During the decompression processes $k_f = k_i/1.8$. In the future, the very same procedure could be followed while changing the stiffness with a shortcut function instead of a step in order to accelerate the relaxation towards equilibrium.

4.1 Levitated particle at equilibrium

First we analyze the data for a nanoparticle trapped at equilibrium at a pressure of 9 mbar.

4.1.1 PSD, radius, mass and calibration.

We follow the steps shown in section 3.3, obtaining the fit of the PSD for the horizontal and vertical motion modes. They are shown in fig 4.1, and from the fit we obtain the parameters of table 4.1:

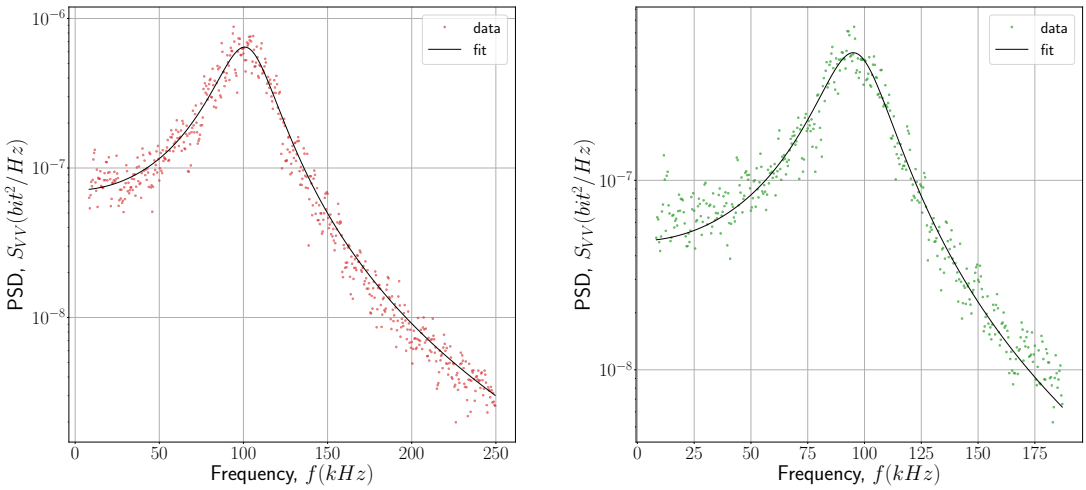

(a) Horizontal motion mode x

(b) Vertical motion mode y

Figure 4.1: Experimental double-sided PSD S_{VV} for the horizontal x (red) and vertical y(green) motion modes. The black line corresponds to fits of eq(3.5) to the experimental data through least squares methods.

Parameter	x	y
f_0 (kHz)	103.73 ± 0.24	97.61 ± 0.23
g (kHz)	34.97 ± 0.59	31.51 ± 0.58
$A \times 10^3$ (bit^2)	431.8 ± 4.9	285.7 ± 3.5
R (nm)	71.06	78.89
m (fg)	2.8 ± 1.0	3.8 ± 1.4
c $(\frac{\text{bit}}{\mu\text{m}})$	11.2 ± 3.4	13.1 ± 4.0
C $(\frac{\text{bit}^2}{\mu\text{m}^2\text{fg}})$ [Eq. (3.10)]	45.35	45.35

Table 4.1: Obtained parameters and errors from the fit f_0, g and A. From this parameters the systematic errors of the calibration factors and the mass have been calculated as explained in section 3.3.1

.

The radius R is computed using eq(3.6) where we introduce the density of the particle provided by the manufacturer $\rho_{part} = 1850 \pm 92\ kg/m^3$, the molar mass of dry air $M = (28.97 \pm 1.45) \times 10^{-3}$ kg/mol, the pressure obtained from the gauge as $P = 9 \pm 1.0\ mbar$ and the damping rate obtained from the fit. Since we cannot measure the temperature inside the vacuum chamber yet, the temperature of the room $T = 293 \pm 10\ K$ has been introduced.

Pressures of $P_x^{fit} = 9.11 \pm 0.13$ mbar and $P_y^{fit} = 9.11 \pm 0.18$ mbar are obtained from the fits by using eq (2.7) and inserting the calculated radius and mass of the

table. The pressure values of the fit are compatible with the value measured with the pressure gauge which is: $P = 9 \pm 1$ mbar.

The masses are computed using $m = 4\pi\rho_{\text{part}}\, R^3/3$ and the obtained R from the table as well as the density of the manufacturer. We obtain $\mathrm{m}_x^{fit} = 2.8 \pm 1.0$ fg and $m_y^{fit} = 3.8 \pm 1.4$ fg. The values are both compatible with the mass provided by the manufacturer $m = 2.83 \pm 0.14$ fg.

Finally we obtain the values for the calibration factor using $c = \sqrt{Am\Omega_0^2/\left(k_{\mathrm{B}}T\right)}$. Here the corresponding masses calculated in the previous steps and the factor A from the fit are used. Find the obtained values in table 4.1.

The systematic errors of the mass and the calibration factor are computed as explained in section 3.3.1.

The fits are implemented to the experimental part of the PSD that is shown in the pictures. We selected this frequency range since for higher and lower frequencies the fit does not match the experimental data.

4.1.2 Instantaneous position and velocity

Through calibration and implementing a manual frequency filter we can obtain the instantaneous position of the nanoparticle. We show it in fig 4.2.

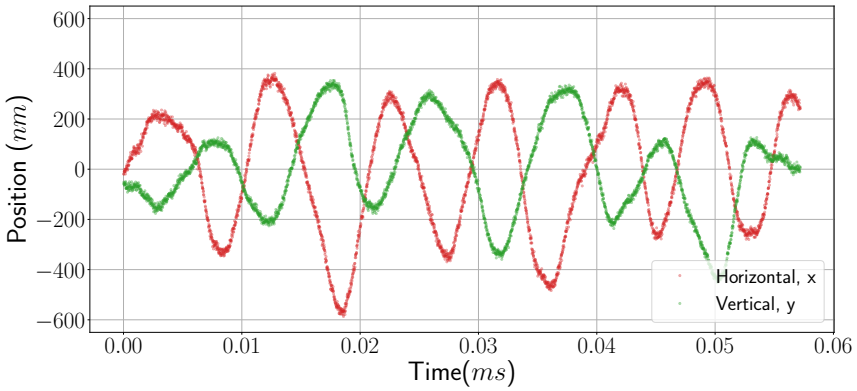

Figure 4.2: Instantaneous position of the horizontal (red) and vertical (green) modes of a levitated particle at equilibrium at a pressure of 9 mbar.

For the manual frequency filter, the position set is splitted in small sub-sets. The average of the sub-vectors is calculated and substracted to the position values.

Due to the random nature of the motion, we average every ten values of the position

in order to compute the velocity. The same sets shown before in fig 4.2 are now averaged and its velocities are calculated and shown in fig 4.3 .

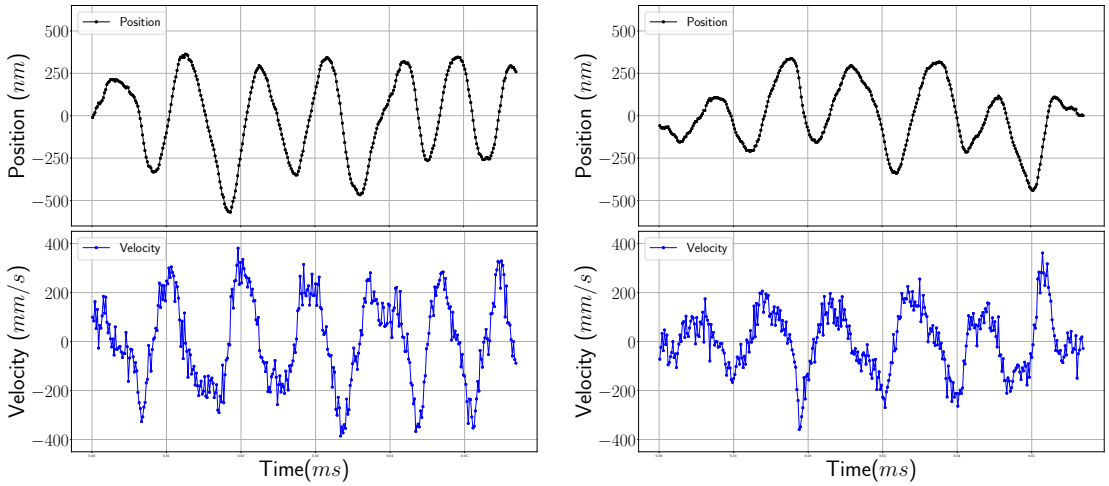

(a) Horizontal motion mode x.

(b) Vertical motion mode y.

Figure 4.3: Averaged position and velocity for a brownian nanoparticle in equilibrium at a pressure of 9 mbar.

Notice first that the velocities are maximum/minimum when the particle position is close to zero. This occurs for the two motion modes at the same time suggesting that at these times the particle is in the center of the well with maximum kinetic energy and minimum potential energy. The sign (positive or negative) of the velocities indicates whether a particles is "going" or "coming" from the center of the well. Notice that this occurs inversely between the two modes.

Notice second that as expected the velocities are zero when the particle oscillates at its maximum amplitude. This occurs as well for the two motion modes at the same time suggesting that at these times the particle is situated in the border of the well containing minimum kinetic energy and maximum potential energy.

4.1.3 Relaxation time and mean square displacement

As explained in section 2.7.3, the relaxation of the levitated nanosphere system is given by the momentum relaxation time, which for units consistency is defined as:

$$\tau_p = \frac{1}{g} = \frac{2\pi}{\Gamma_{CM}}. \tag{4.1}$$

Notice that here g is the regular damping rate while Γ_{CM} is the angular damping rate. According to the obtained values from the fit:

$$\tau_x^{fit} = \frac{1}{g_x^{fit}} = 28.59 \pm 0.49 \quad \mu s \quad ; \qquad \tau_y^{fit} = \frac{1}{g_y^{fit}} = 31.74 \pm 0.60 \quad \mu s. \tag{4.2}$$

We corroborate this calculating the mean square displacement of the nanoparticle in equilibrium as defined in eq (2.14). In order to calculate it we substract every position of a subset $q(t)$ by a fixed initial position $q(0)$ and square the result. Then we use all the subsets to calculate the average of each $(q(t) - q(0))^2$. The result is fitted using again least squares methods with python obtaining the figure 4.4.

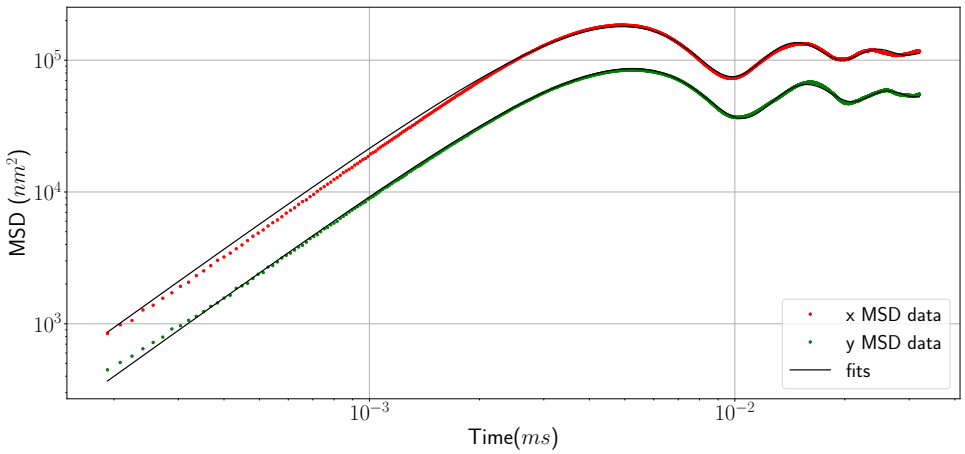

Figure 4.4: The mean square displacements of a silica nanosphere trapped in air at 9 *mbar* for the horizontal mode (red) and vertical mode (green). The lines are the fittings according to Eq. (2.14) leaving as free parameters the relaxation time, the frequency of the particle and the constant $A = \frac{k_B t}{m\Omega_0^2}$.

We used the frequency of the particle, the relaxation time and the constant $A = \frac{k_B t}{m\Omega_0^2}$ as free parameters obtaining new relaxation times of:

$$\tau_x^{MSD} = 28.63 \pm 0.10 \quad \mu s \quad ; \qquad \tau_y^{MSD} = 30.331 \pm 0.090 \quad \mu s. \tag{4.3}$$

While t_x^{fit} and τ_x^{MSD} are compatible, τ_y^{fit} and τ_y^{MSD} are not. This is probably due to the not perfect fit of the MSD in fig 4.4. Nevertheless, they are of the same order and therefore usefull for our practical goals. We intend to observe the relaxation of the variance of the position and velocity distributions in the next section.

Notice in fig 4.4 that as it predicted by the eq (2.14), the amplitude of the oscillations of the MSD decays exponentially with time. Also notice that its oscillation frequency is given by the frequency at which the particle oscillates, which depends on the damping rate and the frequency of the harmonic trap: $\tilde{\Omega} = \sqrt{\Omega_0^2 - \Gamma_{\mathrm{CM}}^2/4}$.

We calculate as well the MSD for shorter timescales $t << \tau_p$ in order to observe evidence of ballistic brownian motion. We find in figure 4.5 that the MSD starts to behave quadratically according to the prediction of eq (2.12) when $t << \tau_p$ which is $(\mathrm{k_B} T_{\mathrm{CM}}/m)\, t^2$. Note that one can observe in fig 4.5b that at times of 10^{-4} ms the MSD starts to show ballistic motion.

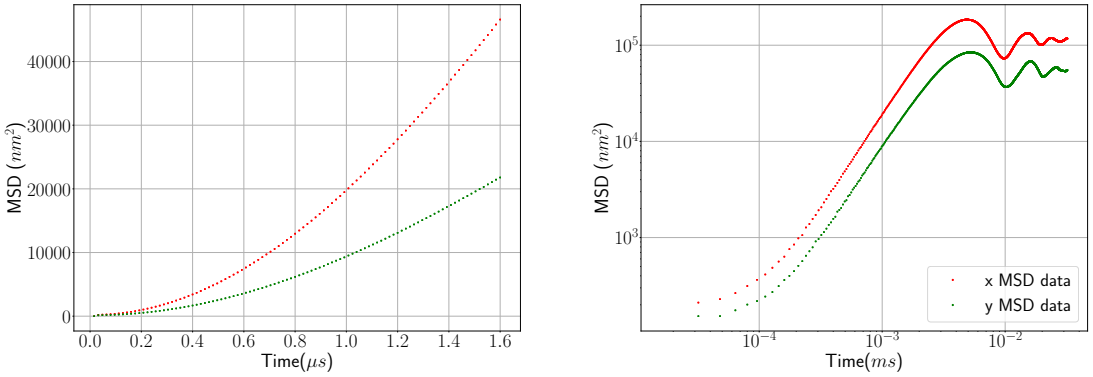

(a) **(b)**

Figure 4.5: MSD data for ballistic motion (a) and for longer time-scales (b). Note that one can observe in b) that at times of 10^{-4} ms the MSD starts to show ballistic motion.

Nevertheless, notice that the vertical axis of figures 4.5 and 4.4 is not correct quantitavely with the theory. We believe this is due to the procedure of computing the MSD that has enlarged the error of the calibration factor.

4.2 Transitory dynamics of a compressed and decompressed nanoparticle.

We present here the results while compressing and decompressing the optical potential of the nanoparticle with a step function. We intend to study the transition behaviour of the dynamics. We first present the calibration of our data. We then study the position and velocity distributions as well as the variation of their variance through time. This is done for the initial state with stiffness k_i and for the final states with stiffness k_f. The behaviour of the variance through time is also compared to the non-modulated case of the previous section in order to appreciate differences. Finally we show plots of the position probability density and of the phase space of the system that might help to analyze the relaxation for longer momentum relaxation times at lower pressures in the future.

4.2.1 PSDs and calibration

We follow here the same procedure explained in section 3.3. Notice nevertheless that in that process it is assumed for the steps followed that the particle must be in equilibrium and we are studying here a non-equilibrium transitory process. For the current matter non-equilibrium dynamics will occur while the nanoparticle changes from the first state to the second. An option to overcome this would be to use for calibration only the compressed and decompressed recorded data after the relaxation time. Nevertheless, this results in using for the PSD only half of the data. We tried this obtaining not good fits for the PSD.

For that reason we use for calibration and the fit of the PSD data similar cuts to the later on analyzed data (see figure 4.9). See code for details. Due to the non-equilibrium process then the calibration quantitative values might not be completely correct for this case, but for the current matter we are interested in the relation between them in order to observe relaxation.

We follow the same steps of section 4.1.1 in order to obtain the fitted PSD now for the 4 cases, of compressed and decompressed. The fits are implemented to the experimental part of the PSD that is shown in figs 4.6 and 4.7. We selected this frequency range since for higher and lower frequencies the fit does not match the experimental data.

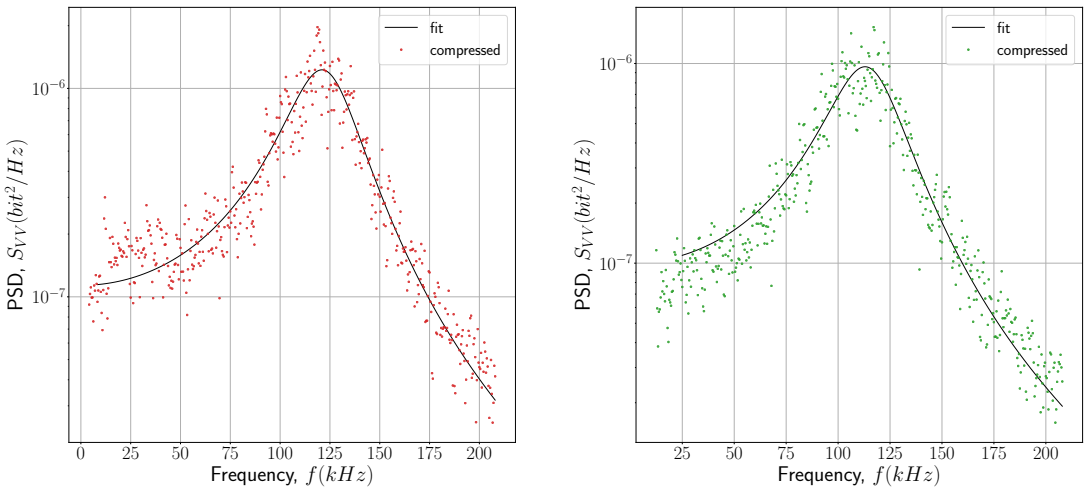

(a) Horizontal motion mode x

(b) Vertical motion mode y

Figure 4.6: Compressed experimental double-sided PSD S_{VV} for the horizontal x (red) and vertical y (green) motion modes. The black line corresponds to fits of eq(3.5) to the experimental data through least squares methods.

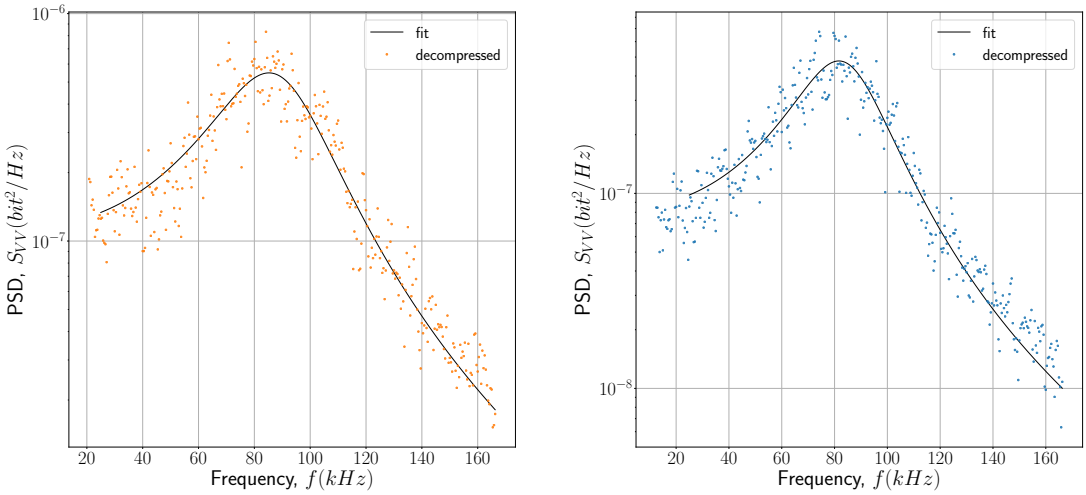

(a) Horizontal motion mode x

(b) Vertical motion mode y

Figure 4.7: decompressed xperimental double-sided PSD S_{VV} for the horizontal x (orange) and vertical y(blue) motion modes. The black line corresponds to fits of eq(3.5) to the experimental data through least squares methods.

The procedure is followed as in section 4.1.1 obtaining the calibration factors. For the compressed case we get:

$$c_x = 19.4 \pm 5.9 \quad \frac{bit}{\mu m}, \qquad c_y = 19.5 \pm 5.9 \quad \frac{bit}{\mu m}. \tag{4.4}$$

While for the decompressed case:

$$c_x = 8.3 \pm 2.5 \quad \frac{bit}{\mu m}, \qquad c_y = 10.4 \pm 3.2. \quad \frac{bit}{\mu m}. \tag{4.5}$$

For comparison we plot them together in fig 4.8. We can appreciate that the signal of compressed PSDs is greater due to the intensity of the laser. A higher stiffness of the optical potential requires a higher intensity of the laser and viceversa.

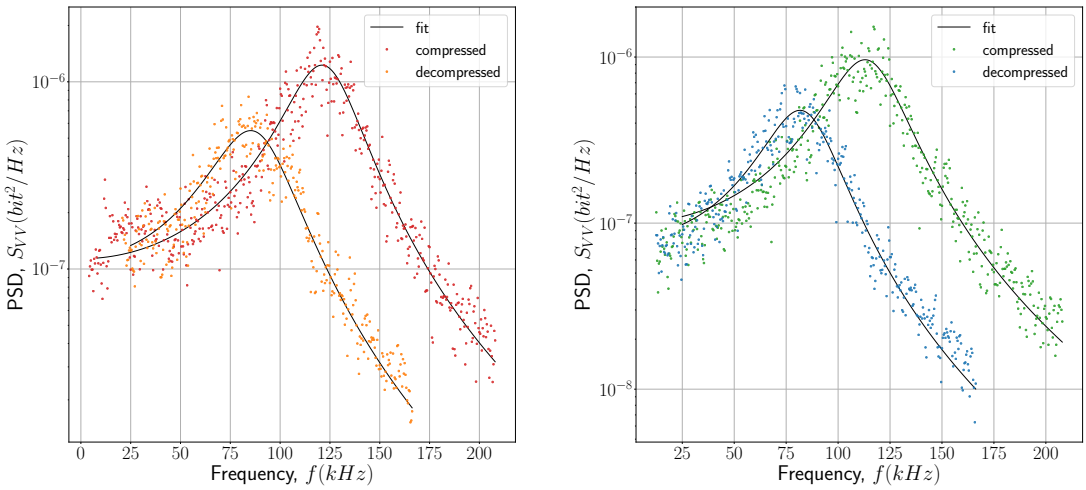

(a) Horizontal motion mode x

(b) Vertical motion mode y

Figure 4.8: Experimental double-sided PSD S_{VV} for the horizontal x (orange and red) and vertical y(blue and green) motion modes. At each of the modes the compressed (red,green) are plotted together with the decompressed cases in order to facilitate its comparison. The black line corresponds to fits of eq(3.5) to the experimental data through least squares methods.

We obtain the following results shown in table 4.2 for the compressed case:

Parameter	x	y
f_0 (kHz)	123.98 ± 0.37	116.12 ± 0.42
g (kHz)	38.14 ± 0.91	37.94 ± 0.90
$A \times 10^3$ (bit^2)	902 ± 14	702 ± 13
R (nm)	71.60	71.94
m (fg)	2.8 ± 1.0	2.9 ± 1.1
c ($\frac{\text{bit}}{\mu\text{m}}$)	19.4 ± 5.9	19.5 ± 5.9
C ($\frac{\text{bit}^2}{\mu\text{m}^2\text{fg}}$) [Eq. (3.10)]	132.21	132.21

Table 4.2: Obtained parameters and errors for a compressed particle. From the fit f_0, g and A. From this parameters the systematic errors of the calibration factors and the mass have been calculated as explained in section 3.3.1

.

And the following results shown in table 4.3 for the decompressed case:

Parameter	x	y
f_0 (kHz)	90.45 ± 0.47	82.66 ± 0.38
g (kHz)	45.82 ± 0.90	37.19 ± 0.94
$A \times 10^3$ (bit^2)	438.1 ± 6.9	702.2 ± 5.1
R (nm)	63.69	74.39
m (fg)	2.00 ± 0.74	3.2 ± 1.2
c ($\frac{\text{bit}}{\mu\text{m}}$)	8.3 ± 2.5	10.4 ± 3.2
C ($\frac{\text{bit}^2}{\mu\text{m}^2\text{fg}}$) [Eq. (3.10)]	34.16	34.16

Table 4.3: Obtained parameters and errors for a decompressed particle. From the fit f_0, g and A. From this parameters the systematic errors of the calibration factors and the mass have been calculated as explained in section 3.3.1

.

Notice again that the mass values are compatible with the mass provided by the manufacturer $m = 2.83 \pm 0.14$ fg for both the compressed and decompressed cases and for both motion modes. Furthermore the obtained pressures from the fit are also compatible with the value obtained with the pressure gauge: $P = 10.0 \pm 1.0$ $mbar$.

4.2.2 Compressed and decompressed position and velocity

In order to compress/decompress the particle, the intensity of the laser is increased in the compressed cycles while decreased in the decompressed cycles. Every compression cycle follows a decompressed one and viceversa. This is done supplying to the EOM a square wave with period of 10 kHz that is created with the function generator. The function generator does not produce a totally clean square wave function and therefore some manipulation of the data is necessary to avoid this effect and confuse it with the relaxation dynamics. In fig 4.9 we show the generated function in black together with the selected position data (blue and green) to analyze the evolution of the variance of the position distribution.

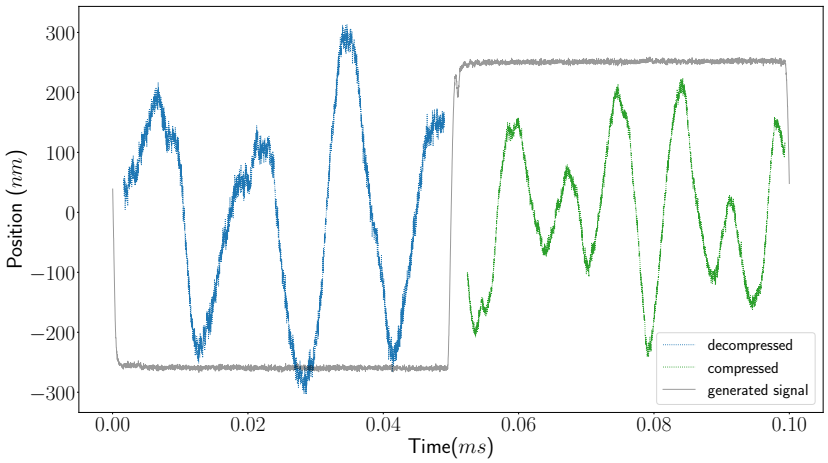

Figure 4.9: Example of selected cuts for the analysis of the decompressed (blue) and compressed (green) vertical position traces of a levitated particle at a pressure of 10 mbar. In black we show the generated function at the times at which it affect the motion of the particle Notice that the vertical axes applies only for the position traces while the generated function is included only to illustrate the times at which the data is cutted for the later treatment.

The averaged position and velocity traces of the horizontal mode of the nanoparticle are shown in fig 4.10. Notice that both the amplitudes are greater for the uncompressed case as expected since while compressing the optical potential we restrict the motion confining the particle.

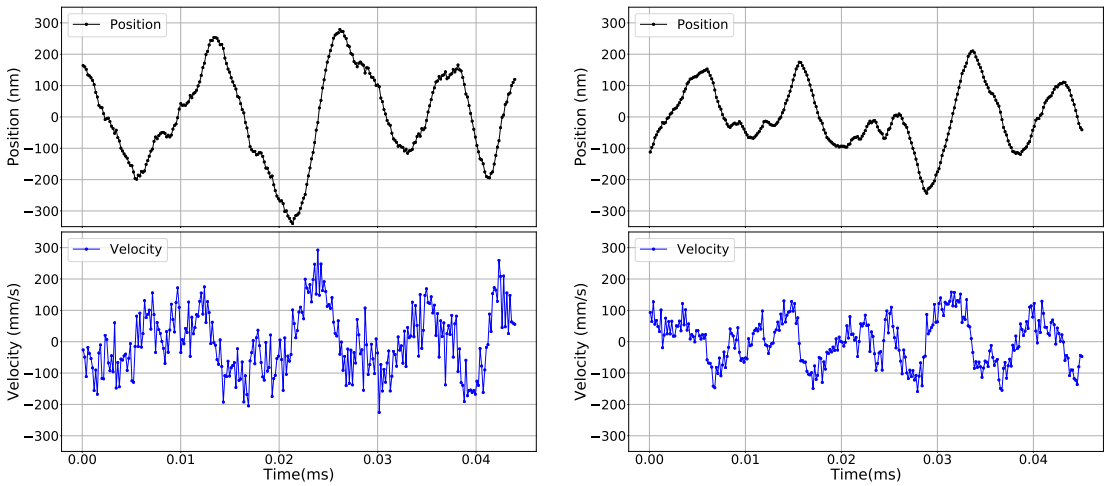

(a) Decompressed traces for the horizontal motion mode. **(b)** Compressed traces for the horizontal motion mode.

Figure 4.10: Averaged position and velocity for a brownian compressed/decompressed nanoparticle at a pressure of 10 mbar.

Also notice that as expected the oscillations are faster for the compressed case. This is intuitive from eq (2.5) since at compressed cycles a higher applied power is given resulting in a higher stiffness and therefore oscillation frequency.

4.2.3 Compressed and decompressed position distribution variance.

We take 1000 compression/decompression cycles, obtaining therefore 1000 trajectories similar to the ones shown in fig 4.10. In order to study the relaxation of the process, we obtain the position distribution at each time making use then of these 1000 position elements and fit it to a gaussian distribution. See the fits in appendix D. The variance of the distribution is extracted at each time and therefore its evolution is analyzed. See first the evolution of the variance for the horizontal mode in fig 4.11. We plotted in red lines the relaxation times obtained from the PSD fits:

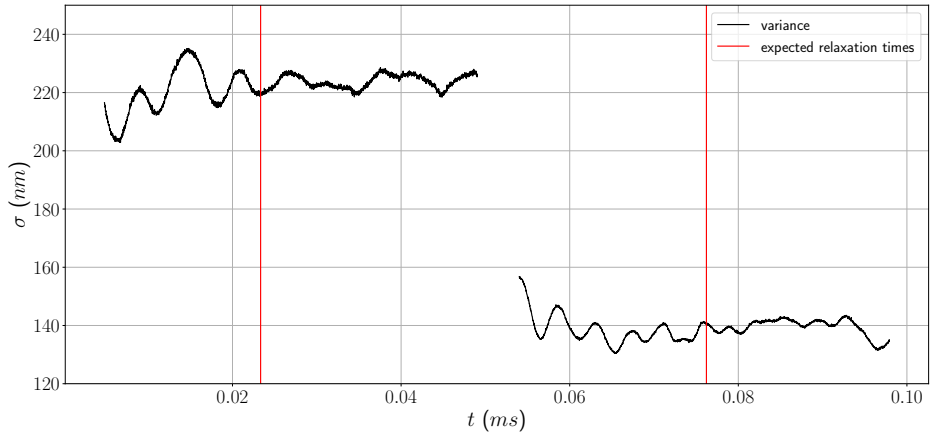

Figure 4.11: Time evolution of the gaussian position distribution variance for the horizontal mode.

Notice first from figs 4.11 and 4.12 that the variance highly decreases for the compressed case since the particle is confined reducing the amplitude of its oscillations.

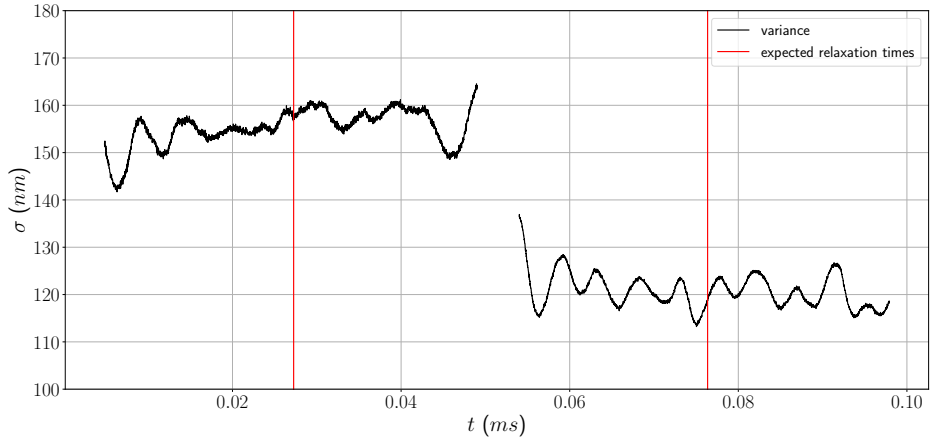

Figure 4.12: Time evolution of the gaussian position variance for the vertical mode.

Notice as well that in both figs 4.11 and 4.12 the mean value of the variance slightly increases for the decompressed cases until arriving the relaxation time while in both compressed cases its mean value decreases. For clarity we plot its relation compared to the equilibrium variance in a logarithmic scale in fig 4.14. We furthermore compare it with the data of section 4.1 plotting the variance evolution for a particle in equilibrium. See fig 4.13. In this cases the mean value of the variance does not increase or decrease.

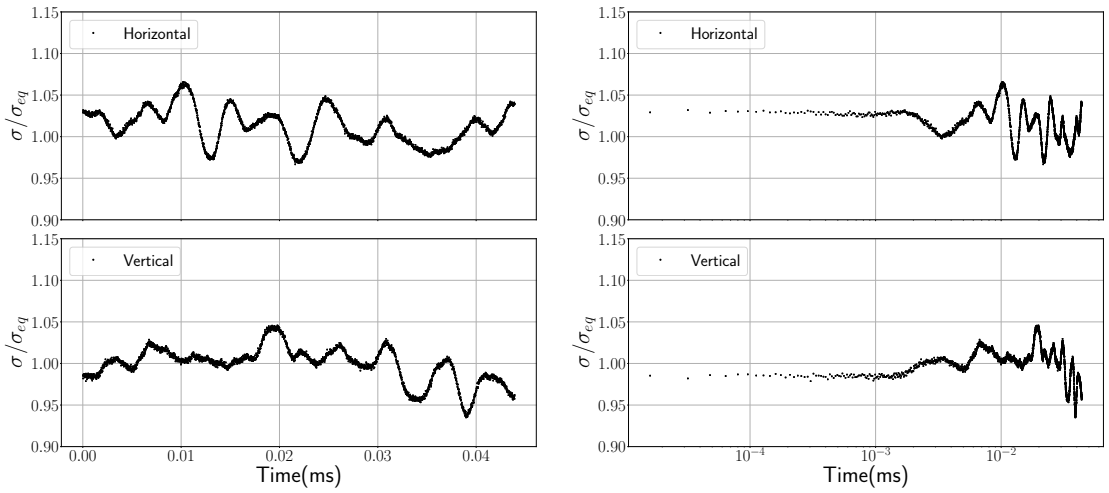

Figure 4.13: Time evolution of the gaussian position variance for a nanoparticle in equilibrium for the horizontal (top) and vertical (bottom) motion modes.

In order to see the evolution of the mean value of the variance we divide it by its equilibrium value and take the logarithmic scale obtaining:

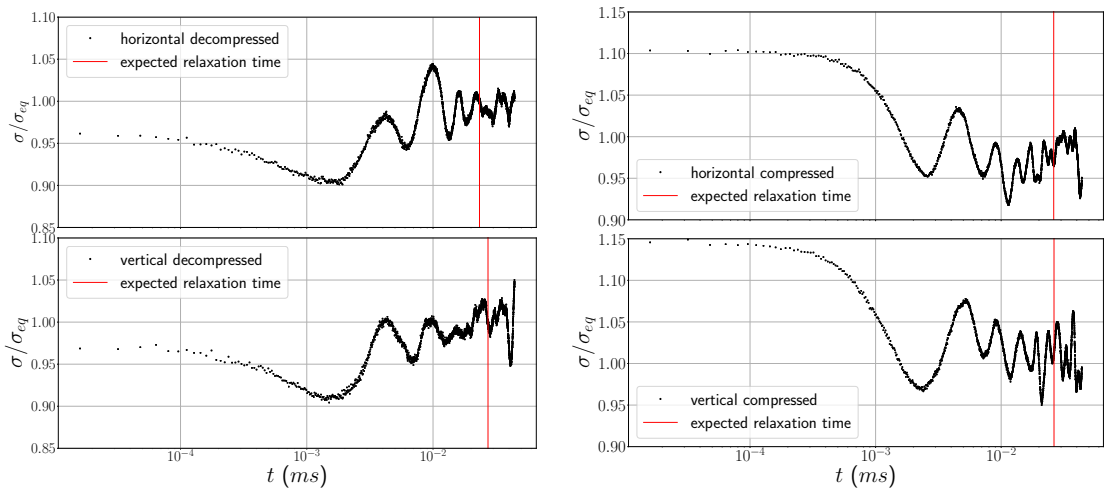

(a) Decompression traces for the horizontal motion mode. **(b)** Compression traces for the horizontal motion mode.

Figure 4.14: Evolution of the position distribution variance for a compressed and decompressed nanoparticle ar a pressure of 10 $mbar$.

We observe that the time-evolution of the position distribution for decompressed

cases variates its mean value a 7% from the beginning to the expected relaxation time. Furthermore the compressed variance variates a 10%. The lower variation of the variance at equilibrium being of less than 5% indicates that there might be signs of the relaxation of the distribution variance. Nevertheless, it is too early to confirm the relaxation due to the small variations.

4.2.4 Phase space

We first show the phase space for the horizontal and vertical modes of a nanoparticle in equilibrium. Fig 4.15 shows that the position distributions are within the limits of the waist of the laser being them of $w_x = 687$ nm and $w_y = 542$ nm for the setup of J. Gieseler where in his phD work he uses a MO with the same numerical aperture as our setup.

While the horizontal mode is mostly homogeneous, the vertical mode phase space is asymmetric, we relate this to the effect of gravity pushing the particle towards the positive direction of our detector see fig 4.15. This indicates therefore that for our data, we are measuring the vertical axis upside-down.

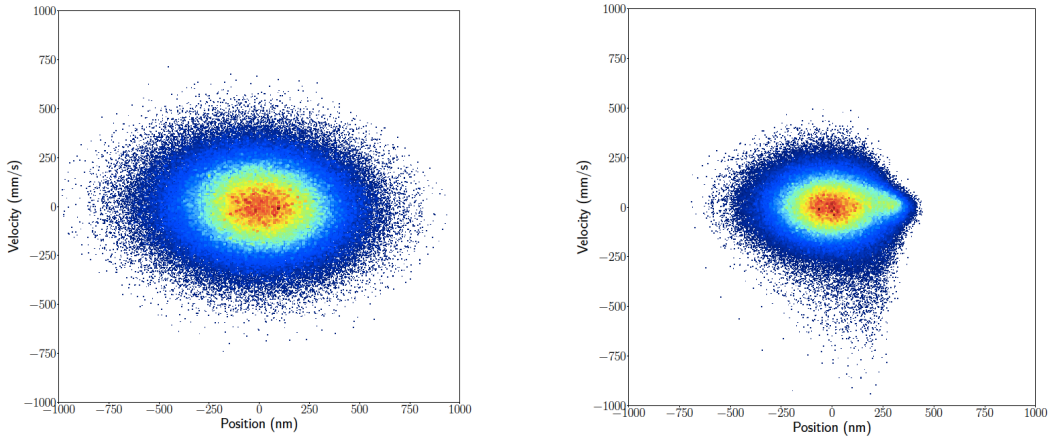

(a) Phase space of the horizontal motion mode x for a particle in equilibrium.

(b) Phase space of the vertical motion mode y for a particle in equilibrium.

Figure 4.15: Histogram of the phase space of a brownian compressed/decompressed nanoparticle at a pressure of 10 mbar. While the horizontal mode is mostly homogeneous.

Notice as well that the vertical mode is more restricted than the horizontal mode showing a difference between the widths of the waste such that $w_x >$w$_y$. These agree as well with the values obtained by Gieseler.

In order to check the effects of compression/decompression on the particle we plot the 2-dimensional phase space distributions for the compressed and decompressed cases in fig 4.16 for the horizontal mode and in fig 4.17 for the vertical mode. Notice that as expected the compressed phase space is confined in the position distribution.

Nevertheless, also as expected the width of the velocity distribution is not affected. This is because there is no energy being removed from the system.

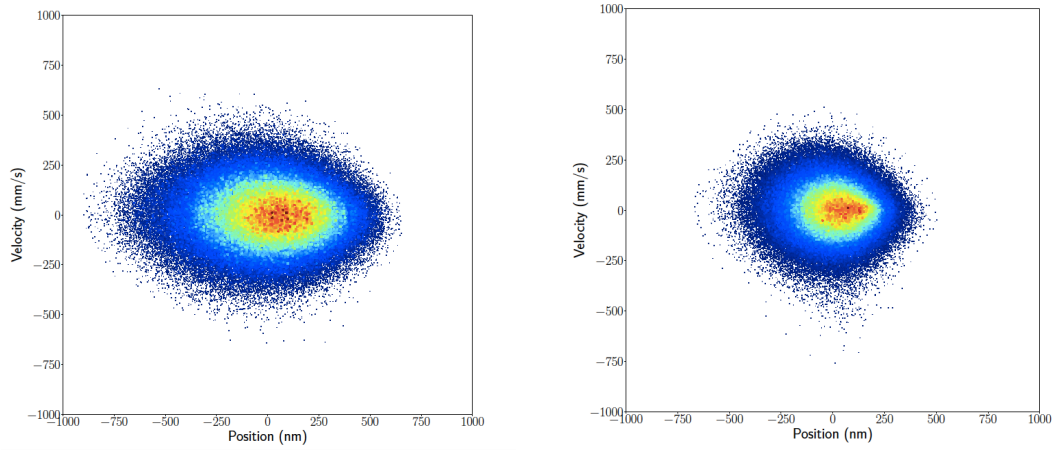

(a) Decompressed phase space of the horizontal motion mode x.

(b) Compressed phase space of the horizontal motion mode x.

Figure 4.16: Histogram of the phase space of a brownian compressed/decompressed nanoparticle at a pressure of 10 mbar.

Notice second that the compression/decompression cycles have deformed the mostly homogeneous phase space for the horizontal motion mode. Furthermore the cycles have suppressed the effect of gravity on the vertical motion mode, see fig 4.17.

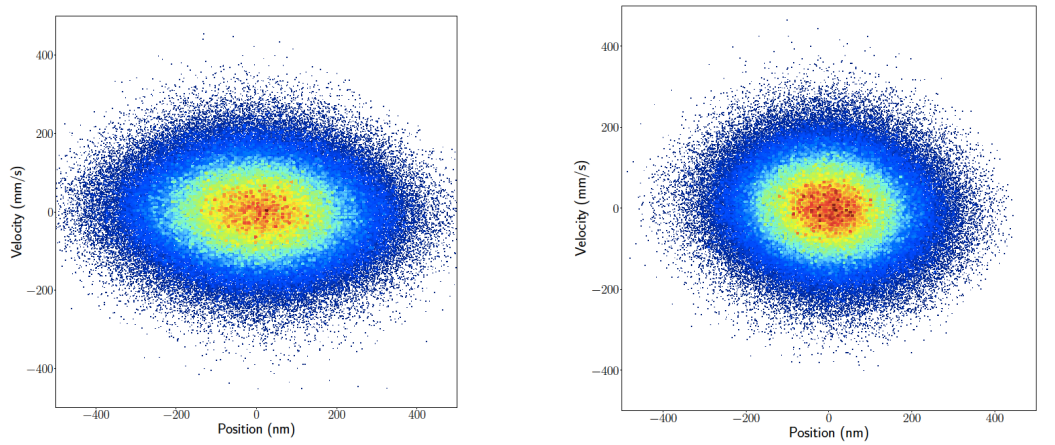

(a) Decompressed phase space of the vertical motion mode y.

(b) Compressed phase space of the vertical motion mode y.

Figure 4.17: Histogram of the phase space of a brownian compressed/decompressed nanoparticle at a pressure of 10 mbar.

Due to the necessity of averaging out of 10 values to obtain the velocities, we do not contain enough points to check the evolution of the phase space through time. Nevertheless, this would be an interesting study in the future in order to compare

the results of our compression/decompression cycles with the theory of squeezing as Vovrosh [49].

Chapter 5

Conclusions

The first steps towards the acceleration on the relaxataion to equilibrium of a levitated particle have been taken.

First of all, we fulfilled our first goal measuring the relaxation time of an optically trapped nanosphere at 10 $mbar$, with an error of less than 2% with respect to its value. Furthermore we obtained compatible values of the relaxation time for a fit of the MSD and showed, at times shorter than the relaxation time, ballistic brownian motion for the first time in the group. The position and velocity for the horizontal and vertical modes of the nanoparticle at equilibrium have been observed at scales of the order and shorter of the relaxation time.

Second, we tracked the position and velocity of a nanoparticle on time-scales shorter than the relaxation time observing a priori the non-equilibrium dynamics of a nanoparticle circulating within two distinct equilibrium states. We did this for compression/decompression cycles, creating two states with different constant stiffness of the optical potential. We observed the time-evolution of the position distribution, obtaining variations of its mean value around 10% that occurred before the obtained relaxation time from the PSD fits. The lower variation of the variance at equilibrium of 5% indicates that there might be signs of the relaxation of the distribution variance. Nevertheless, it is too early to confirm the relaxation without further test that confirm this hypothesis.

Furthermore, as planned, we have looked into the possibilities to implement modulations externally to our levitated particle. We studied how the modulations result in the center of mass dynamics of the particle (see sections 2.5 and 2.3.3) finding interesting applications related to shortcuts and heat engines (main motivation of this master thesis), detection systems and studies of non-linearities of the optical potential see section 2.5.3.

In addition the mass and the calibration factor of an optically trapped nanosphere at 10 mbar has been experimentally obtained with error of 35% and 30% respectively. The large errors suggest that in the future the track of the energy evolution

on the transitory dynamics between equilibrium states would be quantitatively more precise since the error of the mass is avoided (see section 3.3.1).

We also observed experimentally the two-dimensional histogram of the phase space of the nanoparticle corroborating that the motion occurs within the expected limits of the widths of the laser waist $w_x = 687$ nm and $w_y = 542$ nm.

In the future it would be of help to observe the relaxation at lower pressures since longer relaxation times would be obtained and we could observe more oscillations of the nanoparticle per compression/decompression cycle.

We can conclude that we are now in a good position to take the very same steps as given in this work but changing the stiffness through ESE techniques in the transition between two equilibrium states. We are therefore a step closer to pursue the first acceleration to date of the relaxation towards equilibrium of a levitated nanoparticle.

Appendix A

PhD proposal

The proposal hereby presented builds upon my work as part of two different research projects. At the University of Groningen, I worked with Steven Hoekstra, whose group optically levitates silica nanospheres in a strongly focused beam that is externally modulated. At the Universidad Complutense de Madrid, I collaborated with Ignacio A. Martínez who is building protocols to explore shortcuts of relaxation processes and studying colloidal heat engines. Based on these works two goals are presented for this proposal: On the one hand the first experimental implementation of a shortcut on the relaxation to equilibrium of a levitated nanosphere. On the other hand the first construction to date of a heat engine with levitated nanoparticles.

Previous projects
As part of my master project I took part in an experimental effort to levitate nanoparticles in the group of Steven Hoekstra. The initiative aims for using them as mechanical resonators, since they are very sensitive inertial and vibration sensors. We worked on the optimization of the system in order to read out the dynamics and the relaxation of the nanosphere when we modulate its optical potential in time. For that matter I worked on an improvement of the sensitivity when reading out the effect of the modulation on the behaviour of the nanosphere. I studied the foundations to pursue the first experimental implementation of a shortcut on the relaxation to equilibrium of a levitated particle in vacuum. For that purpose, I measured the relaxation time of the system and tracked the motion of the particle at longer and shorter time-scales than this time measuring ballistic brownian motion. Finally I observed signs of relaxation towards equilibrium by compression and expansion of the optical potential stiffness. In addition I perfomed experiments at different pressures and with different modulations as well as treated and analyzed the obtained data with Python.

In parallel at UCM the group of J.R.M. Parrondo studies the use of strategies reminiscent to the theory of shortcuts to adiabaticity [17, 41]. I joined the group in 2019 where, with Ignacio A. Martínez we studied these strategies to accelerate the thermalization of fluids that contain optically trapped micron-sized beads with the

purpose of studying critical Casimir forces.

While Ignacio. A. Martinez works with particles inmersed in fluids to study the overdamped regime, levitated nanospheres can explore the underdamped regime. Both experiments are characterized by the Langevin equation where a brownian particle is trapped with optical tweezers and its motion is driven by a white noise. In this context, a change of the control parameters of the system would upset the state variables that define a particular thermodynamical state. This is the induction of a transition from one state to another.

PhD project

1. The first objective of the PhD proposal lies in an intriguing overlap between both of the projects above exposed. Protocols related to the theory of shortcuts to adiabaticity that were tested by Ignacio A. Martinez [17] in the overdamped regime need to be tested in the underdamped regime [20]. This regime can be explored by levitated nanospheres in high vacuum [15]. Through an inverse engineering the thermalization can be shortcutted in the compression or decompression of a harmonic oscillator from an angular frequency Ω_i to Ω_f, getting an exact scaling solution of the underdamped Fokker-Planck equation.

This part of the project can be achieved within the first year of PhD. Study of theory related to references [17, 20] (3-4 months). Measuring the relaxation for different modulated functions (4 months). Maintenance of the experimental setup (2-3 months). Wrapping up the project (2 months).

By implementing such protocols we would be able to control the state of a levitated nanosphere on unprecedented timescales reaching equilibrium hundreds of times faster than the natural equilibrium rate. Furthermore, the realization of a shortcut has direct applications in the design of efficient nanothermal engines, in the driving of mesoscopic chemical or biological processes and in sensing experiments.

2. The second objective is related to one of the applications of shortcuts to adiabaticity. They can help us improve the efficiency of nanothermal engines optimising their design [41]. Ignacio A. Martinez explored stochastic heat engines in the overdamped regime [28] developing together with J.M.R. Parrondo a Carnot engine [29] .There are theoretical proposals for the underdamped regime that are of interest to be tested with levitated nanospheres [26, 27].

A colloidal stochastic heat engine converts heat flow into mechanical work operating under a cyclic process. The cycle contains two isothermal processes where there is a variation of the potential to extract or implement work and two adiabatic processes with an instantaneous reduction/increase in temperature, see figure A.1. While compression and expansion is achieved by increasing and decreasing the po-

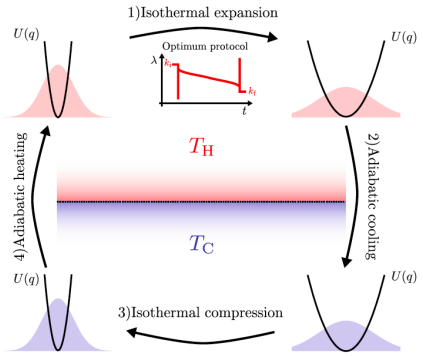

Figure A.1: Stochastic heat engine cycle. Obtained from reference [11]

tential of the harmonic potential that traps the nanospheres, heating and cooling is done by changing the effective temperature of the center of motion particle.

This part of the project can be achieved in the remaining time of the PhD, lasting between 2 and 3 years. Study of theory related to references [26–29] (6-8 months). Testing isothermal processes (4-5 months), Testing adiabatic processes (4-5 months). Testing full cycles (4-6 months). Maintenance of the setup (4-5 months). Wrapping up the project (4 months).

While the overdamped regime has been well explored, the underdamped regime lacks experimental results. It is of interest to check optimal protocols for maximum efficiency at fixed power. Can we determine optimal driving protocols for different values of power? Could we extend the results to include feedback control? Can we explore the quantum regime at high vacuum, and attaining Carnot efficiencies? [30]

Appendix B

Alignment and coupling laser into the polarization-maintaining fiber

It was necessary to increase the amount of laser power that is focused in the vacuum chamber for two reasons:
1. A higher laser power increases the depth of the optical potential facilitating trapping stability.
2. A higher amount of power raised the amount of recorded signal in the photodiodes improving the signal to noise ratio (SNR).
For such matter, I opened the 2nd compartment and played with the 4 mirrors and the X,Y,Z screws of the fiber coupler.

As a result of the coupling, I obtain before the microscope objective and after the PBS cube a power oscillating between 4 and 4.5 mW with OD 2 filter. Nevertheless, the seal of the PM blue fiber to the fiber coupler does not properly fit. By barely touching the fiber we decouple the light loosing a big amount of power.

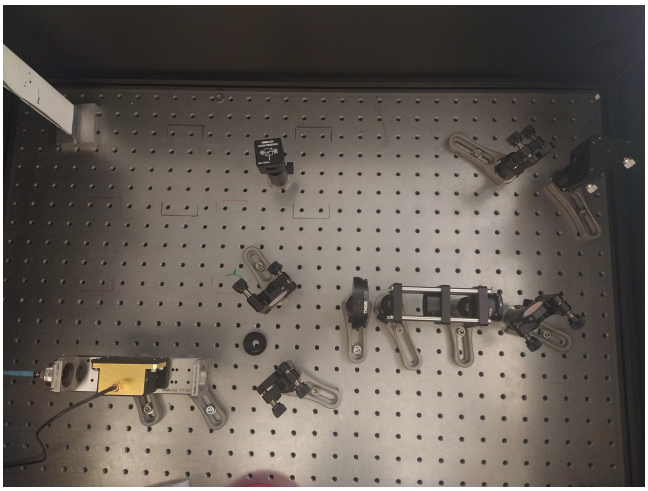

Figure B.1: 2nd comparment of the experimental setup .

The procedure to increase the power was the following:

- 1st: Connect a visible light laser from the output of the blue fiber and collimate it with the Z screws of the fiber coupler lens - As stated before the fiber does not connect properly to the coupler which leave the fiber too far from the fiber coupler lens. This gives no option but to tight the Z screws as much as possible. - I slightly damaged one of the Z screws and decided to replace it from one of the Z screws of the fiber PAF-X15-B

- 2nd: Play with the X-Y screws of the fiber coupler. Use a visible light laser in order to center it at the end of the SingleAxis FiberBench

- 3rd: Maximize power after the galileon telescope. Measure with OD filter after the telescope. First play changing the vertical position of both mirrors (reducing the power with the first mirror and raising with the second or viceversa) and then do the same with horizontal position

- 4th: Maximize power after the fiber with the other 2 mirrors following the same technique as in the previous step. Measure with OD filter after the fiber. If nothing is gotten first check if any light gets out making use of the CCD camera

Appendix C

Dependence of the frequency of the center-of-mass motion on different parameters

We make a qualitative analysis of the FFTs signal changes while changing the polarization, the intensity of the laser and the pressure of the system.

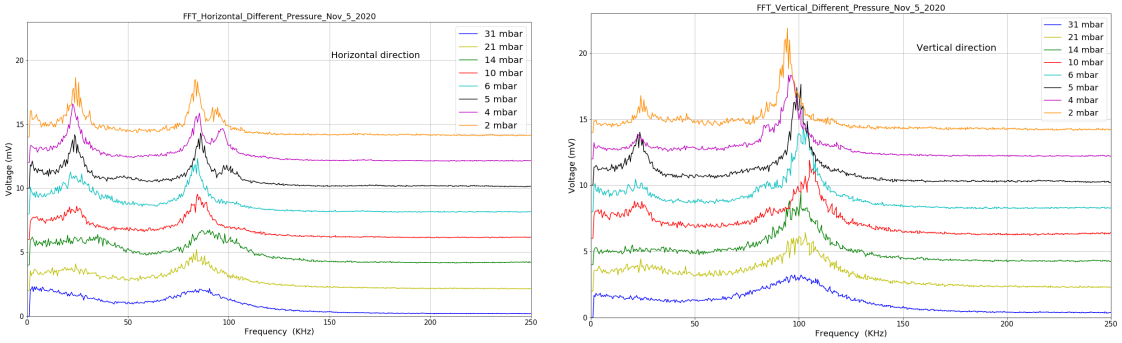

(a) Horizontal mode. **(b)** Vertical mode. FFT changing as a function of pressure

Figure C.1: FFT changing with pressure

Notice that in fig C.1 the FFT are getting stretched for lower pressures due to lower damping rates and therefore higher quality factors. We appreciate as well a change on the frequency mean value of the peak. This might be most likely due to variations of the laser power through time that might be related to the temperature of the laser.

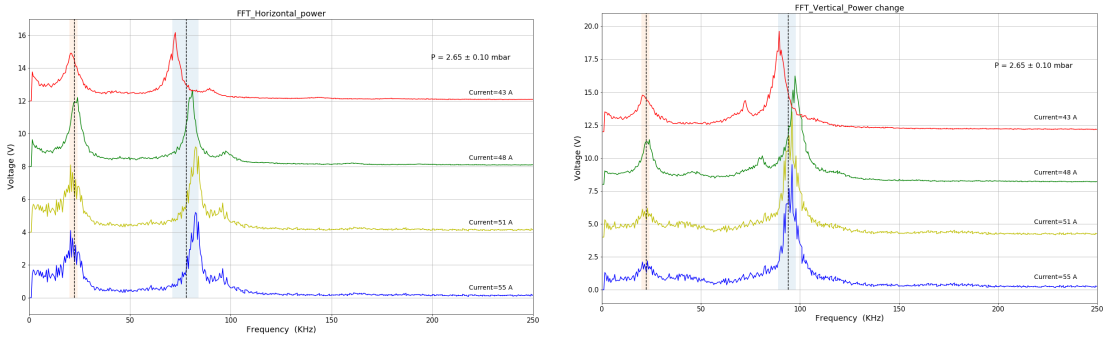

(a) Horizontal mode. **(b)** Vertical mode.

Figure C.2: FFT changing as a function of power

Notice that in fig C.2 we change the current associated with the laser amplifier resulting in a change of the power. notice that for higher currents and therefore powers the frequency increases. This is due to the linear dependence of the frequency on the stiffness and therefore on the intensity and power of the laser.

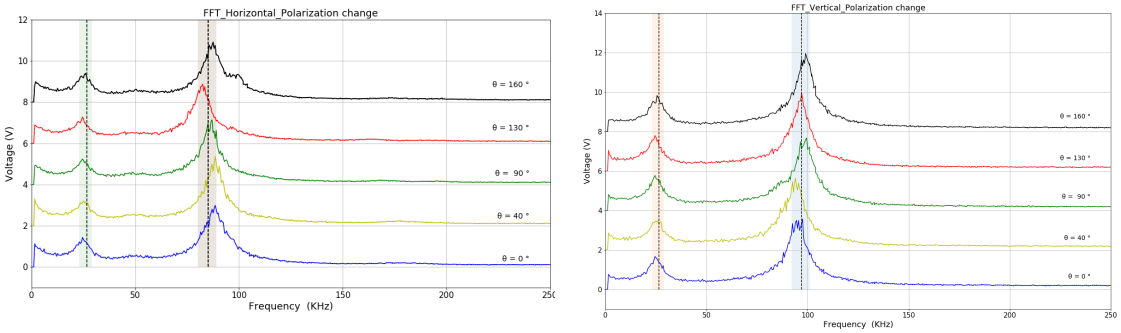

(a) Horizontal mode. **(b)** Vertical mode.

Figure C.3: FFT changing with polarization.

Finally notice that in fig C.3 we use the half wave plate in order to change the polarization of the laser. The variation of the polarization affects inversely at both motion modes as expected from the theory. This is due to that by changing the polarization we change the power contribution of a certain motion mode, therefore the the power is maximum for the vertical mode at vertical polarization and viceversa, see eqs (2.4), (2.5).

Appendix D

Link to the python codes.

There are 4 codes:

- *Nonmod-PSD-fit-MSD*: where we obtain the results of section 4.1
-*Cuts-Calibration* and P-V-Distributions: Where we obtain the results of section 4.2.
- *Cuts-Calibration-1ms*: where we analyze the data for longer times (data when creating a square wave of period of 1ms ten times longer than the results shown in the thesis.)

https://drive.google.com/drive/folders/1uOOdLl69Z4kbNHF16Yaic2TjBLN0RaZx?usp=sharing

Acknowledgements

Special thanks to my supervisor S. Hoekstra for giving me the chance of taking part in the group, which has been the most important step in my career path providing me with enthusiasm and interest in this beautiful topic.
Special thanks as well to A. Sterk for your kind availability and for providing very helpful advices and sources when analysing theoretical papers.
Thank you to M. Morshed for your constant work in the lab, and for teaching me how to use the interesting experimental setup that you built.
Thank you to Kevin and Anno for your constant help when necessary with multiple problems in the lab and programming. Thank you Artem for introducing me to the lab and motivating me in my bachelor project.
Thank you to Nithesh and Manal for pushing me to improve my programming skills.
Thank you to Ignacio A. Martínez for providing interesting ideas on the motivation of my project.
Thank you to the people of the VSI for creating such a pro-active work environment. Thanks Lorenz for interesting conversations, Joost for support, Thomas and Tatiana for kind coffee breaks, and everyone else in the VSI.
Thank you to my family for their constant support.

Bibliography

[1] Markus Aspelmeyer, Tobias J. Kippenberg, and Florian Marquardt. Cavity optomechanics. *Rev. Mod. Phys.*, 86:1391–1452, Dec 2014.

[2] A. Ashkin. Acceleration and Trapping of Particles by Radiation Pressure. *Physical Review Letters*, 24(4):156–159, 1969.

[3] A Ashkin and J M Dziedzic. Feedback stabilization of optically levitated particles. *Applied Physics Letters*, 30(4):202–204, 1977.

[4] A Ashkin, J M Dziedzic, J E Bjorkholm, and Steven Chu. Observation of a single-beam gradient force optical trap for dielectric particles. *Optics Letters*, 11(5):288, 1986.

[5] Richard W Bowman and Miles J Padgett. Optical trapping and binding. *Reports on Progress in Physics*, 76(2):026401, 2013.

[6] Tongcang Li, Simon Kheifets, David Medellin, and Mark G. Raizen. Measurement of the Instantaneous Velocity of a Brownian Particle. *Science*, 328(5986):1673–1675, 2010.

[7] Tongcang Li and Mark G. Raizen. Brownian motion at short time scales. *Annalen der Physik*, 525(4):281–295, 2013.

[8] Vijay Jain, Jan Gieseler, Clemens Moritz, Christoph Dellago, Romain Quidant, and Lukas Novotny. Direct Measurement of Photon Recoil from a Levitated Nanoparticle. *Physical Review Letters*, 116(24):243601, 2016.

[9] Loïc Rondin, Jan Gieseler, Francesco Ricci, Romain Quidant, Christoph Dellago, and Lukas Novotny. Direct measurement of Kramers turnover with a levitated nanoparticle. *Nature Nanotechnology*, 12(12):1130–1133, 2017.

[10] James Millen, Tania S Monteiro, Robert Pettit, and A Nick Vamivakas. Optomechanics with levitated particles. *Reports on Progress in Physics*, 83(2):026401, 2020.

[11] James Millen and Jan Gieseler. Thermodynamics in the Quantum Regime, Fundamental Aspects and New Directions. *Fundamental Theories of Physics*, pages 853–885, 2019.

[12] L. P. Faucheux, L. S. Bourdieu, P. D. Kaplan, and A. J. Libchaber. Optical Thermal Ratchet. *Physical Review Letters*, 74(9):1504–1507, 1995.

[13] Udo Seifert. Stochastic thermodynamics, fluctuation theorems and molecular machines. *Reports on Progress in Physics*, 75(12):126001, 2012.

[14] Jan Gieseler and James Millen. Levitated Nanoparticles for Microscopic Thermodynamics—A Review. *Entropy*, 20(5):326, 2018.

[15] Jan Gieseler, Romain Quidant, Christoph Dellago, and Lukas Novotny. Dynamic relaxation of a levitated nanoparticle from a non-equilibrium steady state. *Nature Nanotechnology*, 9(5):358–364, 2014.

[16] Thai M. Hoang, Rui Pan, Jonghoon Ahn, Jaehoon Bang, H. T. Quan, and Tongcang Li. Experimental Test of the Differential Fluctuation Theorem and a Generalized Jarzynski Equality for Arbitrary Initial States. *Physical Review Letters*, 120(8):080602, 2018.

[17] Ignacio A. Martínez, Artyom Petrosyan, David Guéry-Odelin, Emmanuel Trizac, and Sergio Ciliberto. Engineered swift equilibration of a Brownian particle. *Nature Physics*, 12(9):843–846, 2016.

[18] Anne Le Cunuder, Ignacio A. Martínez, Artyom Petrosyan, David Guéry-Odelin, Emmanuel Trizac, and Sergio Ciliberto. Fast equilibrium switch of a micro mechanical oscillator. *Applied Physics Letters*, 109(11):113502, 2016.

[19] Antoine Bérut, Artak Arakelyan, Artyom Petrosyan, Sergio Ciliberto, Raoul Dillenschneider, and Eric Lutz. Experimental verification of Landauer's principle linking information and thermodynamics. *Nature*, 483(7388):187–189, 2012.

[20] Marie Chupeau, Sergio Ciliberto, David Guery-Odelin, and Emmanuel Trizac. Engineered Swift Equilibration for Brownian objects: from underdamped to overdamped dynamics. *New Journal of Physics*, 20(7):075003, 2018.

[21] Jonghoon Ahn, Zhujing Xu, Jaehoon Bang, Yu-Hao Deng, Thai M. Hoang, Qinkai Han, Ren-Min Ma, and Tongcang Li. Optically Levitated Nanodumbbell Torsion Balance and GHz Nanomechanical Rotor. *Physical Review Letters*, 121(3):033603, 2018.

[22] Stefan Kuhn, Alon Kosloff, Benjamin A Stickler, Fernando Patolsky, Klaus Hornberger, Markus Arndt, and James f. Full rotational control of levitated silicon nanorods. *Optica*, 4(3):356, 2017.

[23] Jan Gieseler, Bradley Deutsch, Romain Quidant, and Lukas Novotny. Subkelvin Parametric Feedback Cooling of a Laser-Trapped Nanoparticle. *Physical Review Letters*, 109(10):103603, 2012.

[24] I.I. Novikov. The efficiency of atomic power stations (a review). *Journal of Nuclear Energy (1954)*, 7(1):125–128, 1958.

[25] F. L. Curzon and B. Ahlborn. Efficiency of a carnot engine at maximum power output. *American Journal of Physics*, 43(1):22–24, 1975.

[26] A. Dechant, N. Kiesel, and E. Lutz. Underdamped stochastic heat engine at maximum efficiency. *EPL*, 119(5):50003, 2017.

[27] Andreas Dechant, Nikolai Kiesel, and Eric Lutz. All-Optical Nanomechanical Heat Engine. *Physical Review Letters*, 114(18):183602, 05 2015.

[28] Ignacio A. Martínez, Édgar Roldán, Luis Dinis, and Raúl A. Rica. Colloidal heat engines: a review. *Soft Matter*, 13(1):22–36, 2016.

[29] I. A. Martínez, É. Roldán, L. Dinis, D. Petrov, J. M. R. Parrondo, and R. A. Rica. Brownian Carnot engine. *Nature Physics*, 12(1):67–70, 2016.

[30] Mohit Lal Bera, Maciej Lewenstein, and Manabendra Nath Bera. Attaining Carnot efficiency with quantum and nanoscale heat engines. *npj Quantum Information*, 7(1):31, 2021.

[31] J. Roßnagel, O. Abah, F. Schmidt-Kaler, K. Singer, and E. Lutz. Nanoscale Heat Engine Beyond the Carnot Limit. *Physical Review Letters*, 112(3):030602, 2013.

[32] Luca Papariello, Oded Zilberberg, Alexander Eichler, and R. Chitra. Ultrasensitive hysteretic force sensing with parametric nonlinear oscillators. *Physical Review E*, 94(2):022201, 2016.

[33] James M L Miller, Dongsuk D Shin, Hyun-Keun Kwon, Steven W Shaw, and Thomas W Kenny. Spectral narrowing of parametrically pumped thermomechanical noise. *Applied Physics Letters*, 117(3):033504, 2020.

[34] Felix Tebbenjohanns, Martin Frimmer, Andrei Militaru, Vijay Jain, and Lukas Novotny. Cold damping of an optically levitated nanoparticle to microkelvin temperatures. *Phys. Rev. Lett.*, 122:223601, Jun 2019.

[35] Gerard P. Conangla, Francesco Ricci, Marc T. Cuairan, Andreas W. Schell, Nadine Meyer, and Romain Quidant. Optimal feedback cooling of a charged levitated nanoparticle with adaptive control. *Phys. Rev. Lett.*, 122:223602, Jun 2019.

[36] Jan Gieseler, Lukas Novotny, and Romain Quidant. Thermal nonlinearities in a nanomechanical oscillator. *Nature Physics*, 9(12):806–810, 2013.

[37] F Ricci, M T Cuairan, G P Conangla, A W Schell, and R Quidant. Accurate Mass Measurement of a Levitated Nanomechanical Resonator for Precision Force-Sensing. *Nano Letters*, 19(10):6711–6715, 2019.

[38] F. Ricci, R. A. Rica, M. Spasenović, J. Gieseler, L. Rondin, L. Novotny, and R. Quidant. Optically levitated nanoparticle as a model system for stochastic bistable dynamics. *Nature Communications*, 8(1):15141, 2017.

[39] Martin Frimmer, Jan Gieseler, Thomas Ihn, and Lukas Novotny. Levitated nanoparticle as a classical two-level atom [Invited]. *Journal of the Optical Society of America B*, 34(6):C52, 2017.

[40] Samuel Aldana, Christoph Bruder, and Andreas Nunnenkamp. Detection of weak forces based on noise-activated switching in bistable optomechanical systems. *Physical Review A*, 90(6):063810, 2014. Instability region.

[41] D Guéry-Odelin, A Ruschhaupt, A Kiely, E Torrontegui, S Martínez-Garaot, and J G Muga. Shortcuts to adiabaticity: Concepts, methods, and applications. *Reviews of Modern Physics*, 91(4):045001, 2019.

[42] Geng Li, H. T. Quan, and Z. C. Tu. Shortcuts to isothermality and nonequilibrium work relations. *Physical Review E*, 96(1):012144, 2017.

[43] Alex Gomez-Marin, Tim Schmiedl, and Udo Seifert. Optimal protocols for minimal work processes in underdamped stochastic thermodynamics. *The Journal of Chemical Physics*, 129(2):024114, 2008.

[44] A. Bérut, A. Petrosyan, and S. Ciliberto. Energy flow between two hydrodynamically coupled particles kept at different effective temperatures. *EPL*, 107(6):60004, 2014.

[45] Marie Chupeau, Benjamin Besga, David Guéry-Odelin, Emmanuel Trizac, Artyom Petrosyan, and Sergio Ciliberto. Thermal bath engineering for swift equilibration. *Physical Review E*, 98(1):010104, 2018.

[46] Erik Hebestreit, Martin Frimmer, René Reimann, Christoph Dellago, Francesco Ricci, and Lukas Novotny. Calibration and energy measurement of optically levitated nanoparticle sensors. *Review of Scientific Instruments*, 89(3):033111, 2018.

[47] David Hempston, Jamie Vovrosh, Marko Toroš, George Winstone, Muddassar Rashid, and Hendrik Ulbricht. Force sensing with an optically levitated charged nanoparticle. *Applied Physics Letters*, 111(13):133111, 2017.

[48] Chris Dawson and James Bateman. Spectral analysis and parameter estimation in levitated optomechanics. *Journal of the Optical Society of America B*, 36(6):1565, 2019.

[49] Jamie Alexander Vovrosh. *Parametric feedback cooling and squeezing of optically levitated particles*. PhD thesis, University of Southampton, June 2018.

[50] P. Welch. The use of fast Fourier transform for the estimation of power spectra: A method based on time averaging over short, modified periodograms. *IEEE Transactions on Audio and Electroacoustics*, 15(2):70–73, 1967.

[51] Kirstine Berg-Sørensen and Henrik Flyvbjerg. Power spectrum analysis for optical tweezers. *Review of Scientific Instruments*, 75(3):594–612, 2004.

[52] Poul Martin Hansen, Iva Marija Tolic-Nørrelykke, Henrik Flyvbjerg, and Kirstine Berg-Sørensen. tweezercalib 2.1: Faster version of MatLab package for precise calibration of optical tweezers. *Computer Physics Communications*, 175(8):572–573, 2006.